Accepted Manuscript

Substitution and diffusion of Cr^{2+} and Cr^{3+} in synthetic forsterite and natural olivine at 1200-1500 °C and 1 bar

M.C. Jollands, H.St.C O'Neill, J. Van Orman, A.J. Berry, J. Hermann, M. Newville, A. Lanzirotti
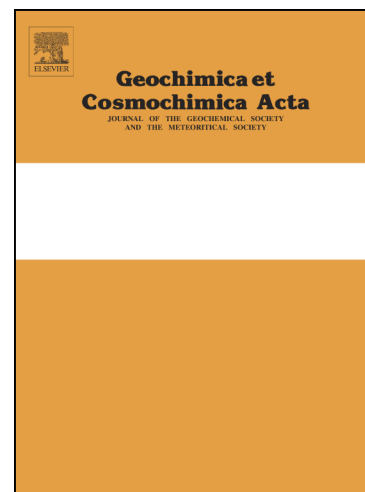
Please cite this article as: Jollands, M.C., O'Neill, H.St.C, Van Orman, J., Berry, A.J., Hermann, J., Newville, M., Lanzirotti, A., Substitution and diffusion of Cr^{2+} and Cr^{3+} in synthetic forsterite and natural olivine at 1200-1500 °C and 1 bar, *Geochimica et Cosmochimica Acta* (2017), doi: https://doi.org/10.1016/j.gca.2017.09.030

Substitution and diffusion of Cr^{2+} and Cr^{3+} in synthetic forsterite and natural olivine at 1200-1500 °C and 1 bar

Jollands, M.C.[1,2], O'Neill, H.St.C[1], Van Orman, J.[3], Berry, A.J.[1], Hermann, J.[1,4], Newville, M.[5], Lanzirotti, A.[5]

[1]Research School of Earth Sciences, Australian National University, Canberra, ACT2601, Australia

[2]Institute of Earth Sciences, Géopolis building, University of Lausanne, 1015 Lausanne, Switzerland

[3]Department of Geological Sciences, Case Western Reserve University, 10900 Euclid Ave, Cleveland, OH 44106, USA

[4]Institute of Earth Sciences, University of Bern, Baltzerstrasse 3, 3012 Bern, Switzerland

[5]Center for Advanced Radiation Sources, The University of Chicago, Chicago, IL 60637, USA

[[**note to typesetters**: aSiO$_2$ and fO$_2$, used throughout, are sub sub, i.e. a_{SiO_2} and f_{O_2}]]

Abstract

The diffusion and substitution mechanisms and Cr in forsterite were studied as a function of crystallographic orientation and the chemical potentials of all four components in the system MgO-SiO$_2$-Cr-O. Oxygen fugacity (fO$_2$) was varied over 15.4 log units at 1400 °C and was fixed at iron-wüstite equilibrium for a temperature

series (1200-1500 °C). The valence state changes of Cr along some diffusion profiles was also investigated using X-ray absorption near edge structure spectroscopy.

Cr diffusion was found to be anisotropic (fastest along the c axis), and considerably faster in the presence of protoenstatite (high silica activity, aSiO$_2$) than in the presence of periclase (low aSiO$_2$). Cr diffusion profiles were longer at lower fO$_2$ with more extreme diffusive anisotropy at higher fO$_2$. Determined Cr diffusion coefficients were similar to those of Fe-Mg inter-diffusion in olivine at equivalent conditions. The diffusivity of Cr was found to be a function of its own concentration, but, as an approximation, Cr diffusion (in m^2/s) along the c axis of pure forsterite, at an fO$_2$ corresponding to iron-wüstite at 200 µg/g Cr could be described using:

$$\log D_{Cr} = -4.37 \pm 0.26 \text{ m}^2\text{/s} + \frac{-316 \pm 8 \text{ kJ/mol}}{2.303 \text{ RT}}$$

where R is the gas constant in kJ/Kmol and T is the temperature in Kelvin.

In forsterite, the valence state ratio of chromium (Cr^{2+}/ΣCr, where ΣCr= Cr^{2+}+Cr^{3+}) changed systematically along diffusion profiles. The equilibrium Cr^{2+}/ΣCr ratio imposed by the fO$_2$ of the experiment was observed at the diffusion interface, and this changed to a constant value in the crystal interior.

Cr^{3+} always substitutes onto an octahedral site in olivine. At high aSiO$_2$, Cr^{3+} uses M site vacancies ([vac]) for charge balance (i.e. Cr$^{3+}_{4/3}$[vac]$_{2/3}$SiO$_4$), whereas at low aSiO$_2$ a new mechanism was observed with charge balance achieved by Mg^{2+} on the tetrahedral site producing a 'spinel type' substitution, Cr$^{3+}_2$MgO$_4$. Cr^{2+} always substitutes directly for Mg^{2+}, forming the Cr$^{2+}_2$SiO$_4$ substitution.

Comparative experiments using San Carlos olivine showed slightly faster Cr diffusion, a lesser concentration dependence of diffusion and no Cr valence state change along diffusion profiles.

1 Introduction

Diffusion in olivine exerts control over mantle rheology (e.g. Ricoult and Kohlstedt, 1985), electrical conductivity (e.g. Karato, 1990) and retention of trace and major element signatures in melt inclusions (e.g. Gaetani and Watson, 2000; Spandler et al., 2007). Frozen diffusion profiles can yield timescales of volcanic and magmatic processes (e.g. Costa and Dungan, 2005; Peslier et al., 2015; Ruprecht and Plank, 2013) and rates of diffusion partially determine closure temperatures of radiogenic dating systems (Dodson, 1973; Ganguly and Tirone, 1999, 2001). Therefore, it is not surprising that the effects of pressure, temperature, oxygen fugacity (fO$_2$), chemical activity (e.g. aSiO$_2$) and isotopic mass on diffusion in olivine have been thoroughly investigated (Brady and Cherniak, 2010; Chakraborty, 2010 and references therein), such that diffusion in olivine has become a synecdoche of diffusion in silicates in general.

However, there remains an interesting, but potentially complex phenomenon that has yet to be directly investigated in any systematic way, that is, how a cation occurring in more than one valence state diffuses. For studying this phenomenon, which should provide a new and novel perspective on diffusion in silicates in general, olivine again provides an interesting opportunity.

Chromium has been shown to exist in natural olivine in two oxidation states, both octahedrally coordinated on the M-sites. Cr^{3+} dominates in terrestrial settings (Bell et al., 2014), and Cr^{2+} has been found in lunar and meteoritic olivine (McKeown et al., 2014; Sutton et al., 1993), and olivine and ferropericlase found in diamond-hosted inclusions (Burns, 1975; Odake et al., 2008). Both Cr^{2+} and Cr^{3+} have been

incorporated into olivine experimentally (Bell et al, 2014; Hanson and Jones, 1998; Schreiber and Haskin, 1976). In addition, Cr^{4+} may occur in tetrahedral coordination in synthetic olivine (e.g. Akhmetzyanov et al., 2013; Rager et al., 1991; Yen and Jia, 1995), and Cr^{6+} is stable in olivine-bearing synthetic melts equilibrated at high oxygen fugacity (Berry and O'Neill, 2004). In melts, the transition between predominantly Cr^{2+} and predominantly Cr^{3+} occurs in the geologically-relevant region between the quartz-fayalite-magnetite and iron-wüstite equilibria (Berry and O'Neill, 2004; Berry et al., 2006). The diffusivity of Cr in olivine is also important for determining the closure temperature of the ^{53}Mn-^{53}Cr dating scheme (Lugmair and Shukolyukov, 1998, Ito and Ganguly, 2006).

From the experimental perspective, studying the diffusion of Cr in olivine offers a number of advantages:

1) The system MgO-SiO_2-Cr_2O_3 (i.e. MgO-SiO_2-Cr-O at high fO_2) is simple; forsterite is in equilibrium with magnesiochromite and either protoenstatite or periclase at 1400 °C (Keith, 1954). The equilibrium parageneses of natural Fe-bearing olivine are essentially the same, existing with magnesiochromite and either orthopyroxene or ferropericlase.

2) The transition between Cr^{2+} and Cr^{3+} has been well studied in Fe-free melts at 1400 °C where forsterite is a liquidus phase (by Berry and O'Neill (2004)).

3) The solubility of Cr in olivine at 1400 °C is on the order of 100s μg/g to wt.% (Li et al., 1995; Mallmann and O'Neill, 2009), allowing routine measurements using laser ablation inductively coupled plasma mass spectrometry (LA-ICP-MS) and electron probe microanalysis (EPMA), and permitting the determination of Cr valence states by X-ray absorption near edge structure (XANES) spectroscopy.

4) Diffusion of Cr in olivine can be fast enough to produce long (100s µm) concentration-distance profiles in short (days to weeks) times at >1200 °C (Spandler and O'Neill, 2010).

5) The transition between pure Cr^{2+} and Cr^{3+} takes place over an easily accessible (using CO_2-CO gas mixes) range of fO$_2$ (Berry and O'Neill, 2004; Berry et al., 2006). Characterising the solubility and diffusivity of an element with multiple valences requires not only determination of concentration, but also the ratio of the relevant valence states. In this study, concentrations were determined using LA-ICP-MS and EPMA, and the valence state ratio using XANES spectroscopy. This allows a simple concentration-distance profile to be resolved into its components and aids understanding of kinetically mediated valence state interaction and diffusion pathways.

The paper is structured as follows. LA-ICP-MS data is treated before XANES spectra, as we move from relative simplicity (Cr considered alone) to complexity (Cr considered as Cr^{2+} and Cr^{3+}). Within each section, interface concentrations are treated first, then diffusion is second. Considering equilibrium helps us to understand the substitution mechanisms, which then guides the interpretation of diffusion profiles.

2   Method

2.1   Basic experimental design

The experimental design followed that described in Zhukova et al. (2014) and Jollands et al. (2014) and then used by Jollands et al. (2016a, 2016b) and Zhukova et al. (2017), which is advantageous as it allows full buffering of chemical activities in trace and minor element diffusion experiments. All experiments were undertaken at

the Australian National University, except the pre-anneal series (described below), which was conducted at the University of Lausanne.

A large single crystal of forsterite grown by the Czochralski method (Solix Corporation (Belarus)) was cut into oriented cubes (oriented using growth faces and characteristic Si-O overtones in polarised Fourier-transform infrared spectra) with a diamond-impregnated 150 μm low-speed circular saw. The composition of this crystal is documented in Zhukova et al. (2014); the main contaminants are Al and Co (20-30 μg/g). San Carlos olivine cubes were cut from a large (~1 cm^3) crystal oriented by X-ray diffraction (guided by cleavage planes (weak) that are generally parallel to (010) or (100) in olivine). The cubes were mounted in epoxy, ground flat on p1200 SiC paper, polished using 6, 3 and 1 μm diamond paste on cloth laps, then removed from the epoxy and cleaned.

The experiments conducted with pure forsterite investigated the system MgO-SiO_2-Cr-O (i.e. MgO-SiO_2-Cr_2O_3-CrO), with the chemical potentials of the four components specified by the diffusant source using three-phase solid assemblages, and the fO_2 buffered by the gas phase. The fO_2 was mostly set by CO-CO_2 gas mixes, or using air to achieve a high fO_2 (fO_2 of air at 1 bar is $10^{-0.7}$ bars, regardless of temperature) and CO in equilibrium with graphite to achieve a low fO_2. The experimental fO_2 was calculated on the basis of the gas mixing ratio alone. The fO_2 imposed by the CO-CO_2 mix is occasionally verified in our laboratory using an yttria stabilised zirconia sensor that replaces the usual sample holder. The degradation in the performance of such sensors with prolonged use at high temperatures (i.e. >1400 °C) and low fO_2 militates against continuous monitoring of fO_2 during experiments (e.g. O'Neill and Pownceby 1993).

With four components and three phases, plus one externally-controlled chemical potential (fO$_2$), the system is fully buffered according to the phase rule. There are two three-phase assemblages in the system MgO-SiO$_2$-Cr-O in equilibrium with forsterite (Mg$_2$SiO$_4$) that are stable over most of the range of fO$_2$ investigated, namely forsterite-protoenstatite-magnesiochromite (fo-prEn-mcr) and forsterite-periclase-magnesiochromite (fo-per-mcr). See Table 1 for these and other abbreviations used in this text. These three-phase assemblages were synthesised from SiO$_2$, MgO and Cr$_2$O$_3$ powders that were dried, weighed and mixed for ~2 h under acetone in an automated agate mortar, before being pressed into pellets, loosely wrapped in Pt wire and sintered in a gas mixing furnace under a 50-50 CO-CO$_2$ mix at 1400 °C for 48 h. X-ray diffraction was used to determine that all required phases were present in the sintered pellets, which were then ground into powders.

The powders were mixed with polyethylene oxide glue and pasted onto the polished crystal surfaces. Residual water was removed by drying at ~100 °C overnight, and the crystal-powder couples (usually six, comprising two buffering assemblages and three crystallographic orientations) were placed onto a ~12 mm square Pt tray and hung from an alumina rod in a gas mixing furnace, generally under CO-CO$_2$ mixes.

The charges were heated to the experimental temperature at 6 °C per minute and held there for 1-39 days, before rapid cooling by simply lifting them out of the furnace. The heating up and cooling down times were negligible relative to the experimental durations. The experimental temperatures were monitored externally using type B Pt-Rh thermocouples.

The buffer powders were easily removed from the crystals after the experiments. In a few cases (extreme fO$_2$ conditions) the presence of the initial buffering phases was again verified using powder X-ray diffraction, which confirmed that no phase changes

had taken place. The crystals were then cut in half (perpendicular to the diffusion

interface) then mounted in epoxy, with the cut side facing out, and polished for LA-

ICP-MS and XANES spectroscopy (with the latter only used for the 1400 ºC fO_2

series experiments).

2.1.1 Oxygen fugacity series at 1400°C

The majority of experiments were conducted in this series, in which fO_2 was varied

over 15.4 log units at 1400 °C (see Supplementary Table 1 for experimental

conditions). The majority of experiments were run using CO-CO_2 gas mixes.

For the experiments conducted in air (the highest fO_2 used), the crystal-buffer couples

were placed in crimped 5 mm diameter Pt tubes lightly packed with Cr source

powder, to minimise the effect of Cr loss by volatilisation.

For the lowest fO_2 condition investigated in this study, equivalent invariant

assemblages were made of forsterite-protoenstatite-carbide-graphite and forsterite-

periclase-carbide-graphite mixes, where carbide refers to chromium carbide, Cr_3C_2

(crb), the phase stable with graphite in the Cr-C system (Venkatraman and Neumann,

1990). These experiments were annealed in CO gas, using a graphite holder

constructed following the design of O'Neill and Berry (2006).

Experiments were also conducted using San Carlos olivine. For these, three-phase

assemblages were constructed in a similar way to those used in the forsterite

experiments, but with added Fe (as Fe_2O_3) in order to form olivine, Mg-rich chromite

and either orthopyroxene or magnesiowüstite with appropriate Mg/Fe ratios to be in

major-element equilibrium with the San Carlos olivine. Powdered San Carlos olivine

was also added to the mix. Although the experiments with San Carlos olivine have an

additional major-element component (Fe), the chemical potentials are also fixed at a

given P and T at equilibrium since the Mg/Fe ratios of all phases are specified by the fixed Mg/Fe ratio of the bulk composition.

2.1.2 Temperature series at fixed fO$_2$

Experiments were conducted between 1200 and 1500 °C at fO$_2$ corresponding to the Fe-FeO equilibrium to determine the temperature dependence of diffusivity. These experiments were run for 4-39 days (longer time at lower temperature). Generally, six crystals were run simultaneously, except for the 1200 °C experiment, which did not include b and a axis experiments with the fo-per-mcr buffer).

2.1.3 Time series

Time series experiments ('t' in Supplementary Table 1) were run for one, three, six and 9.6 days (the longest experiment was CODE5) in c axis oriented crystals using the fo-prEn-mcr buffer. For the one, three, six day experiments, the charges were placed into the furnace together, and after one day, the furnace temperature was dropped to 1000 °C (within around 30 min), all three charges were removed together, one crystal was removed from the box, the other two placed back into the furnace, and the temperature ramped up to 1400 °C again at 6 °C/min. These steps were repeated after two more days, and the experiment was terminated after a further three days.

2.1.4 Buffer composition series

In order to verify that it is the chemical activities rather than the concentrations of components in the buffers that control diffusivity, four buffers were synthesised in the fo-prEn-mcr field with various MgO:Cr$_2$O$_3$:SiO$_2$ ratios. The buffers contained 10, 25, 40 and 55 wt.% Cr$_2$O$_3$ and however much SiO$_2$ and MgO was necessary to keep the

compositions approximately equidistant from the fo-mcr and prEn-mcr tielines in the

$MgO-Cr_2O_3-SiO_2$ ternary. These were pressed into pellets, sintered, annealed, then

powdered, glued onto the surfaces of three *c* axis oriented pure forsterite crystals, and

annealed together ('Buffer' series in Supplementary Table 1).

2.1.5 Pre-anneal tests

Four crystals of forsterite, with the same orientation ((010) polished, *b* axis

perpendicular), but with different pre-anneal histories, were annealed with the same

Cr buffer at the same T-fO$_2$ conditions, to test whether their different histories had any

effect on diffusion profiles. All pre-anneals were conducted at 1400 °C, in CO_2, for 48

hours. The first crystal was pre-annealed alone, with unknown aSiO$_2$ (placed in a Pt

wire basket). The second was pre-annealed packed in a forsterite-enstatite powder

(synthesised from >99.99% purity MgO and SiO_2) and the third was pre-annealed in

periclase powder. The pre-anneals were conducted separately to avoid any potential

contamination. The fourth crystal was not pre-annealed at all. All four crystals were

then coupled to fo-prEn-mcr powder, and annealed for 7 days at 1400 °C in pure CO_2.

2.2 Analytical methods

2.2.1 LA-ICP-MS

All LA-ICP-MS analyses were conducted in scanning mode – no depth-profiling was

done in this study. Analyses were conducted using a LambdaPhysik Compex ArF

excimer laser coupled to an Agilent 7700 ICP-MS via He-Ar carrier gas at the

Australian National University. The laser beam was a 6x100 μm rectangle, scanned

across the crystal at 1 μm per second from low to high Cr concentration (core to rim),

as described by Spandler and O'Neill (2010) and used by Jollands et al. (2014; 2016a,

2016b, 2016c) and Zhukova et al. (2014) for characterising similar profiles. As described above, the surface from which the analyses were taken was only exposed post-diffusion anneal. The small width of the slit gives high spatial resolution in the direction of diffusion, and the length of the slit maximises the volume of material ablated. A Cr Kα X-ray map collected at the Advanced Photon Source (Figure 1) on a typical crystal shows that contributions from the other faces of the target crystal are negligible, so the relatively poor spatial resolution (compared to other analytical techniques) is not a concern, and diffusion can still be considered one-dimensional. Laser energy was maintained around 50 mJ at the point of exit, and the pulse rate was 5 Hz. ^{52}Cr, ^{53}Cr , ^{27}Al, ^{57}Fe, ^{25}Mg and ^{29}Si were all counted for 0.01-0.2 s. Data were processed using Iolite (Paton et al., 2011) with NIST SRM 610 glass as the primary and NIST SRM 612 as the secondary standard, using the values of Jochum et al. (2011). Critical values (lowest detectable concentrations) for Cr using ^{53}Cr, calculated using the Ulianov et al. (2016) formulation and assuming Gauss-approximated (excess variance) backgrounds, were typically 0.1-0.2 μg/g. High baselines for ^{52}Cr (possibly ^{36}Ar^{16}O) meant that data from this isotope could not generally be used. Concerns have been raised regarding the usefulness of NIST glass as a Cr standard due to compositional heterogeneities in the glass towards the edges of discs (Eggins and Shelley, 2002). As a precaution, all the analyses of the NIST glass standard were obtained from near the centre of the disc, and the occasional analysis that showed possible heterogeneity was discarded and another collected elsewhere on the glass.

2.2.2   EPMA

Data was collected using EPMA from a single diffusion profile that shows the total range of Cr contents observed in this study (0-1.1 wt% Cr; CODE3, fo-prEn-mcr, *b*-axis) using a Cameca SX100 electron probe at the Australian National University. Mg and Si Kα fluorescence were counted on TAP, and Cr Kα fluorescence was simultaneously counted on PET, LLIF and LPET crystals. The accelerating voltage and beam current were 15 keV and 100 nA, with 150 s and 75 s counting times on peak and background, respectively, to give estimated limits of detection around 50-70 µg/g. San Carlos olivine and chromite were used as calibration standards.

The main purpose was to determine whether LA-ICP-MS analyses were compromised by matrix effects. The EPMA/LA-ICP-MS comparison (Supplementary Figure 1) shows that matrix effects are not a concern in this system.

Compared to our LA-ICP-MS method, EPMA gives slightly better spatial resolution, but this advantage needs to be balanced against the higher limit of detection. There is also the potential problem of phantom effects when measuring Cr at low concentrations adjacent to material containing Cr at high concentrations, due not only to secondary X-ray fluorescence but also stray electrons and Bremstrahlung (see Fig. 2 of Hermann et al. (2005)). This problem was avoided in the present study by physically removing the powder of the buffering assemblage before mounting the crystal, but this might not be in other experiments where the buffering assemblage may sinter onto the crystal, in which case the buffer could be removed by gentle abrasion. The practical difference is that the EPMA profile took >8 hours to acquire, versus ~6 minutes for the LA-ICP-MS profile.

2.2.3 XANES spectroscopy

XANES spectra were recorded in fluorescence mode at GeoSoilEnviroCARS (GSECARS) beamline 13IDE of the Advanced Photon Source Argonne National Laboratory, USA. The excitation energy was selected using a cryogenically-cooled Si(111) monochromator, resulting in a spectral energy resolution of ~ 1.25 eV when coupled with the core-hole width. The energy was calibrated by defining the first peak in the derivative spectrum of Cr foil (recorded in transmission mode) to be at 5989.2 eV. High energy harmonics were removed by Rh-coated Kirkpatrick-Baez mirrors that were used to focus the beam to ~ 1 x 2 μm. Samples were mounted at 45˚ to both the incident beam and a four element Si drift fluorescence detector (Hitachi Vortex ME4); the distance between the detector and the sample was adjusted along a diffusion profile to maintain an approximately constant incoming count rate that was within the linear range of the detector. The fluorescence counts from the silicon drift detector were processed using XIA XMap digital signal electronics. All spectra were corrected for detector dead time. Spectra were recorded from 5939 to 6370 eV with a step size of 5 eV for the baseline (5939-5979 eV), 0.2 eV for the pre-edge and edge (5979-6014 eV) and grading from 1.5 to 6 eV above the edge. The total spectral acquisition time was ~ 12 min. Spectra were normalised to the incident photon flux (I_0) measured with a 250 mm long helium-filled ion chamber upstream of the focusing mirrors. The resulting spectra were deglitched manually and compared after subtraction of a constant baseline and normalisation to the average intensity above 6055 eV.

The samples were presented in the same epoxy mounts as used for LA-ICP-MS and EPMA. As the X-rays penetrate into the sample, spectra are derived from a volume defined by the beam size (1 x 2 μm) on the sample surface and an exponentially

decreasing intensity going into the crystal. The samples were therefore oriented such that the beam path was parallel to the (001) plane and hence normal to the c axis (Figure 2). Spectra were recorded along the diffusion profiles at intervals of between 10 and 50 μm, depending on the rate at which the spectra were changing with distance. In general, the intervals were more widely spaced near to the crystal-buffer interface and more closely spaced towards the low concentration end of the diffusion profiles. For most points only one spectrum was acquired but at lower Cr concentrations (less than ~100 μg/g) replicate spectra were recorded and averaged. It should be noted that while the crystallographic orientations of the diffusion profiles were known, the orientation of the sample as mounted and polished was random. For example, considering that diffusion was measured along [001]), the surface on which analyses were made could be (010) or (100) or anything in between. The samples can therefore be considered as partially orientation matched to one another (and therefore to the end member experiments).

For an anisotropic material such as forsterite, XANES spectra may vary with crystallographic orientation (Supplementary Figure 3). Thus, previously reported Cr K-edge XANES spectra of Cr^{2+}- and Cr^{3+}-containing forsterite powders (Sutton et al. 1993) are not appropriate standards. Instead, the partially orientation-matched samples in which the Cr was expected to be nearly all Cr^{2+} (fO$_2$ imposed by graphite-CO), or nearly all Cr^{3+} (air) were used as end-members.

2.3 Diffusion modelling

Three methods were used for modelling diffusion. The first two were used for bulk Cr measurements (LA-ICP-MS measurements, corroborated by EPMA), and the third only for Cr^{3+} as determined by XANES spectroscopy.

Where Cr diffusion profiles were found to have the shape of the error function, the relevant analytical solution to the diffusion equation was used assuming constant interface composition, one-dimensional diffusion and a semi-infinite crystal (modified from Crank, 1973):

$$C(x,t)=C_{core}+(C_{rim}-C_{core})\times erfc\left(\frac{x}{\sqrt{4Dt}}\right) \tag{1}$$

$C(x,t)$ is the concentration (C) at distance from the interface x (m) and time t (s), C_{rim} and C_{core} are the Cr concentrations ($\mu g/g$) at the interface and in the background crystal respectively, and D is the diffusion coefficient, in m^2/s, assumed, in this case, to be independent of concentration. In practice, this was only applicable to profiles at the lowest fO_2 where all Cr is Cr^{2+}, and to some periclase buffered experiments. All other profiles deviated from the error function in a non-negligible way.

Most diffusion profiles deviated from the error function towards a 'hockey stick' shape, suggesting Cr diffusivity is dependent on its own concentration. The theory of concentration-dependent diffusion is well developed:

$$\frac{\partial C(x,t)}{\partial t}=\frac{\partial}{\partial x}\left\{D(C)\frac{\partial C(x,t)}{\partial x}\right\} \tag{2}$$

where $D(C)$ is D as a function of C. Eq. (2) expands to:

$$\frac{\partial C(x,t)}{\partial t}=\frac{\partial D}{\partial x}\times\frac{\partial C(x,t)}{\partial x}+D\frac{\partial^2 C(x,t)}{\partial x^2} \tag{3}$$

In this study, we use a one-dimensional finite differences scheme, (e.g. Costa et al., 2008):

$$C_{i,j+1}=C_{i,j}+\Delta t\left(\frac{D_{i+1,j}-D_{i,j}}{\Delta x}\right)\left(\frac{C_{i+1,j}-C_{i,j}}{\Delta x}\right)+D_{i,j}\Delta t\left(\frac{C_{i+1,j}-2C_{i,j}+C_{i-1,j}}{\Delta x^2}\right) \tag{4}$$

Fitting was generally done by subsampling a three, five or seven-point moving average (depending on profile length), and altering Δx and Δt to satisfy the Courant condition ($D\Delta t/\Delta x^2 <0.5$) at the highest diffusion coefficient (at the interface). Cr

interface and background concentrations were kept constant during the fitting. The diffusion coefficient was then allowed to vary as some function of Cr concentration. Several types of relationships between Cr concentration and diffusion coefficient were tried, with inverse exponential decay giving the best fit to the data. Thus, a purely empirical relationship was used:

$$\log D_{Cr} = \log D_{Cr,max} - (\Delta \log D_{Cr}) e^{-[Cr]/m} \tag{5}$$

with $\Delta \log D_{Cr}$, $\log D_{Cr,max}$ and m being fitting parameters. $\log D_{Cr}$ is the logarithm (base 10) of the diffusion coefficient of Cr, $\Delta \log D_{Cr}$ is the potential variation in $\log D_{Cr}$ as a function of concentration, $\log D_{Cr,max}$ is the highest diffusion coefficient (sometimes extrapolated), [Cr] is the concentration of Cr, in μg/g, and m describes the steepness of the curve in $\log D_{Cr}$, [Cr] space.

However, given that Cr diffusion profiles are generally expected to be comprised of both Cr^{2+} and Cr^{3+} (Bell et al., 2014), the simple, empirical approximation that fits total Cr profiles may useful in terms of application (given that generally Cr is measured as an element rather than Cr^{2+} or Cr^{3+}) but not in terms of point defects. Therefore, we also fitted Cr^{3+} profiles, measured by XANES spectroscopy, to a relationship that describes the concentration dependence of diffusion of M^{3+} cations alone, including the binding energy between M^{3+} and its associated vacancy (discussed below). This was derived by Van Orman et al. (2009) for trivalent cation diffusion in periclase and altered for the different ionic configuration in olivine. Profiles were fitted to this relationship only where XANES spectroscopy data were available, i.e. the fO$_2$ series at 1400 °C.

The diffusivity of M^{3+} at each discrete point along the profile is defined by:

$$D_{M^{3+}} = D_2 \left\{ \frac{3}{4} - \left(\frac{X_{M^{3+}}^2}{16} + \frac{3X_{M^{3+}}}{4K_2} + \frac{1}{4(K_2)^2} \right)^{-1/2} \left(\frac{X_{M^{3+}}}{16} + \frac{3}{8K_2} \right) \right\}$$ (6)

where $D_{M^{3+}}$ is the diffusion coefficient of the diffusing trivalent cation at given

concentration and D_2 is the diffusion coefficient of the cation-vacancy pair. The

concentration of trivalent Cr is included as $X_{M^{3+}}$, the mole fraction of M^{3+} (Cr^{3+} in

this case) on M sites. It was also necessary to assume a background trivalent

concentration in the forsterite on the order of 7 μg/g in order to fit the profiles.

The term K_2 is defined by (7):

$$K_2 = Z_2 \exp \left(\frac{-G_2}{RT} \right)$$ (7)

where Z_2 is the number of nearest neighbour M sites and G_2 is the cation-vacancy

binding energy. The relationship was originally derived for periclase with a relatively

simple cubic (fcc) structure where each M-site cation has 12 nearest neighbours,

rather than the more complex hexagonal olivine (hcp) structure where M1 site cations

have 4 nearest neighbours and 8 second-nearest neighbours. Only nearest neighbours

are taken into account for simplicity. Taking the second nearest neighbours into

account would change the absolute binding energies, but not the relative differences

between them. In addition, the model is limited in that it is derived for periclase,

(cubic) so cannot fully describe diffusion in the anisotropic forsterite structure.

3   Results

3.1   Interface concentration and diffusion of Cr (LA-ICP-MS results)

All results pertaining to the interface concentration and diffusion of Cr, prior to consideration of Cr as Cr^{2+} and Cr^{3+}, are given in Tables 2 and 3 that describe enstatite-buffered and periclase-buffered experiments, respectively.

3.1.1   Total Cr concentrations at the interface

The Cr concentrations at the crystal-buffer interface are presented in Table 2 and Table 3. Figure 3 shows the relationship between Cr interface concentration and aSiO$_2$ as a function of fO$_2$ and T. The first order observation is that Cr interface concentrations are consistently higher in protoenstatite-buffered than periclase-buffered experiments, i.e. higher Cr at higher aSiO$_2$.

The Cr interface concentrations increase as experimental fO$_2$ decreases, excluding the lowest fO$_2$ (carbide-buffered) experiment (Figure 3a). The interface concentration of the magnesiowüstite-buffered San Carlos olivine experiment deviates from the trend established by the experiments on forsterite. The interface Cr concentration also increases with experimental temperature (Figure 3b), whilst maintaining the relative difference between interface concentrations from experiments buffered at the two aSiO$_2$ conditions.

3.1.2   Cr diffusion at 1400 ℃

3.1.2.1   Diffusion profile shapes

Diffusion profile geometries are not constant between experiments. When buffered by fo-prEn-mcr (high aSiO$_2$), at high fO$_2$, the diffusion profiles are broadly *concave-up*, approaching the error function (Figure 4a). The high aSiO$_2$ profiles approach a

hockey stick shape (Figure 4c) at low fO$_2$, with the shape not changing as a function of temperature (compare Figure 4f to 6c). At very low fO$_2$ (Figure 4e), the profiles become error-function shaped. The high aSiO$_2$ experiment in San Carlos olivine shows a geometry intermediate between hockey stick and concave-up (Figure 4b). In experiments buffered by fo-per-mcr (low aSiO$_2$), the concentration-distance profiles go from slightly concave-up at high fO$_2$ to slightly concave-down at low fO$_2$ (Figure 4d).

3.1.2.2 *Effect of aSiO$_2$*

Profiles are consistently longer at higher aSiO$_2$ than at low aSiO$_2$. Figure 4c and d show profiles from the same experimental run, buffered by fo-prEn-mcr and fo-per-mcr, respectively. The difference between diffusivity from the different buffers is greatest at low fO$_2$ – the difference in logD$_{Cr,max}$ is an order of magnitude at fO$_2 = 10^{-11.1}$ bars, and half an order of magnitude at fO$_2 = 10^{-0.7}$ bars (air). The effect of aSiO$_2$ on diffusion is seen in both pure forsterite and San Carlos olivine.

3.1.2.3 *Diffusive anisotropy*

Cr diffusion is anisotropic in all experiments, with the c axis having the fastest diffusivity, then b, then a, in line with the findings of Ito and Ganguly (2006). Anisotropy is greatest at high fO$_2$, and lowest at low fO$_2$ (Supplementary Figure 2). The difference in diffusion coefficients is around 100x at high fO$_2$ and 10x at low fO$_2$.

3.1.2.4   Effect of fO_2

Decreasing oxygen fugacity leads to increased profile lengths, with the exception of the lowest fO_2 experiment that resulted in the shortest diffusion profiles. Decreased fO_2 is also associated with an increase in Cr concentration at the interface. Whilst profile lengths increase considerably from the experiment conducted in air to that conducted at the lowest fO_2, using both the fo-prEn-mcr and fo-per-mcr buffers, the diffusivity at any given Cr concentration actually decreases slightly (Figure 5), with a minimum in the experiment conducted at $fO_2 = 10^{-7.6}$ bars (QFM-1.3) at low Cr concentrations. In general, two domains can be distinguished: at $fO_2 = 10^{-6.8}$ bars (QFM-0.5) and higher fO_2, Cr diffusion is around half an order of magnitude faster than in experiments conducted at lower fO_2. The variations of diffusion coefficients within the low and high fO_2 domains are relatively small, except for the $fO_2 = 10^{-7.6}$ bars and the $fO_2 = 10^{-16.1}$ bars experiments.

3.1.2.5   San Carlos olivine versus pure forsterite

Cr diffusion is slightly faster in San Carlos olivine than in pure forsterite (Supplementary Figure 4), both when buffered at high and low $aSiO_2$. Only one experiment was conducted using San Carlos olivine, so it is not known if this difference is maintained at other T-fO_2 conditions. The difference in diffusion coefficients is around half an order of magnitude. In addition, the profile geometries are not the same - at low $aSiO_2$ the Cr profile in San Carlos olivine can be fitted to the error function, whereas the profile in forsterite is concentration-dependent (Table 3). The change in geometry in high $aSiO_2$ experiments is similar, but less extreme.

3.1.2.6 Time series

Measured diffusion profiles in forsterite from the time series at constant temperature (1400 ºC), fO$_2$ (10$^{-9.6}$ bars), aSiO$_2$ (prEn buffered) and orientation (c axis) are shown in Supplementary Figure 5 along with extracted diffusion coefficients, which should be time-independent in a purely diffusive regime. The three, six and 9.6 day experiments yield very similar diffusion coefficients, while the one day experiment gives diffusion coefficients around 0.1 orders of magnitude slower. This change is very small (within the uncertainty of many published diffusion studies), but even if significant, it appears that the Cr diffusion coefficient reaches a constant value after one or two days - shorter than any of our experiments. Pre-anneal series

Our tests suggest that pre-annealing, or not, has no effect on the length or shape of diffusion profiles, nor on the Cr concentration at the interface (Supplementary Figure 6). Retrieved diffusion coefficients are indistinguishable within error.

3.1.2.7 Buffer composition series

Measured diffusion profiles from the buffer composition series are shown in Supplementary Figure 7, along with their buffer compositions (as weighed) in the MgO-SiO$_2$-Cr$_2$O$_3$ ternary. All buffers were in the fo-prEn-mcr field. There is no distinguishable difference between the four different profiles despite the large difference in buffer composition.

3.1.3 Cr diffusion as a function of temperature

The diffusivity of Cr (at fO$_2$ corresponding to Fe-FeO and in pure forsterite) increases with temperature. The nature of the profiles, with diffusion coefficients changing as a function of Cr concentration, means that a single Arrhenius relationship cannot be

developed, rather D must be described as a function of temperature at different Cr concentrations.

Curves describing D_{Cr} are presented in Figure 6 and Supplementary Table 2 at a series of Cr concentrations that straddle the normal range encountered in most natural olivine. D_{Cr} is always higher at high aSiO$_2$ than low aSiO$_2$, and increases with Cr concentration. In addition, the activation energy (steepness of curve) increases systematically as Cr concentration decreases.

3.2 Interface concentrations and diffusivity of Cr^{2+} and Cr^{3+} (XANES spectroscopy results)

3.2.1 XANES end member spectra

From the spectra recorded, three end members were identified based on their peak positions and edge structure (Figure 7a, with interface spectra from experiments in the fO$_2$ series presented in Figure 7b.). The lowest energy edge was observed in the spectrum obtained from the interface of the most reduced experimental products in both aSiO$_2$ buffering conditions (fo-prEn-crb-graph and fo-per-crb-graph). This spectrum has an intense peak at 6005 eV, and no pre-edge feature, and was assigned to Cr^{2+} in octahedral coordination, i.e. Cr$_2^{2+}$SiO$_4$. Tetrahedrally coordinated Cr is generally associated with a pre-edge feature (Pantelouris et al., 2004) that was not observed in these spectra.

The interface spectrum from the most oxidised, high aSiO$_2$ experiments shows a less prominent peak and a higher energy (+~5eV) edge than the spectrum assigned to Cr^{2+}. The weak pre-edge feature, and comparison with similar spectra from Berry and O'Neill (2004) and Bell et al. (2014), suggests this spectrum corresponds to Cr^{3+} in octahedral coordination i.e. Cr$_{4/3}^{3+}$[vac]$_{2/3}$SiO$_4$.

The third end member spectrum was observed at the tail (crystal interior) end of periclase-buffered diffusion profiles at high fO$_2$. In these samples the spectra recorded closest to the crystal interface have their edge at an energy between those of the first two end members. Further into the crystal, the edge moves to lower energy, then reverses direction and shifts to higher energy than that of the interface spectrum. This last spectrum, which does not change over some distance, comprises the third end member, as it cannot be generated by a linear combination of the other two end members. The spectrum has a higher energy white line than the two other end members, and an intense shoulder on the edge. There is also a very weak pre-edge feature. The line shape and energy are nearly identical to that of Cr spinel (Berry and O'Neill, 2004), suggesting that the substitution mechanism has a similar arrangement of cations, with Cr^{3+} in octahedral coordination charge-balanced by Mg^{2+} in an adjacent tetrahedral site i.e. Cr$_2^{3+}$MgO$_4$. As very few XANES spectra were recorded from periclase-buffered experiments, they will not be discussed further.

3.2.2 Cr^{2+} and Cr^{3+} concentration at the interface

With the three end member spectra determined, it was then possible to determine Cr^{2+}/ΣCr for all spectra by linear combination fitting using least-squares regression of the data between 5980 and 6030 eV, with all points weighted equally. The higher spectral resolution between 5980 and 6014 eV weights the fit towards this region. The errors were estimated using the square root of the estimated variance of the random error (1σ) by the *nls* package in the R open-source code. Initially, we assumed that Cr^{2+}/ΣCr at the buffer/crystal interface was 0 for the experiment conducted in air, and 1 at graphite-CO. Subsequent refinement by fitting all the fo-prEn-mcr buffered interface spectra (Figure 7) to the theoretical expression for the variation of Cr^{2+}/ΣCr

with fO$_2$ gave Cr^{2+}/ΣCr of 0.98 for the experiment at graphite-CO, and 0.01 for the experiment in air (see eq. (26) and associated discussion for derivation). There were insufficient data to warrant such a refinement with the periclase-buffered experiments.

Assuming that the Cr^{2+}/ΣCr ratio is the same at the true interface as at the closest measurement position ~3 µm away (assuming a perfectly aligned 6 µm wide laser slit), the interface concentrations of Cr^{2+} and Cr^{3+} were then determined using the Cr concentrations extracted from curve-fitting of LA-ICP-MS data. The concentrations of Cr^{2+} and Cr^{3+} away from the interface were calculated using Cr^{2+}/ΣCr ratios and five- to seven-point averages of Cr concentrations from LA-ICP-MS data. Interface Cr^{2+}/ΣCr, Cr^{2+} and Cr^{3+} are given in Table 4, along with results pertaining to the diffusivity of Cr^{3+}-vacancy pairs.

From Table 4, two general trends pertaining to interface concentrations are clear. The first is that the concentration of Cr^{3+} at the diffusion interface is always the same, around 1200 µg/g, regardless of fO$_2$, except in the very low fO$_2$ experiment where Cr$_3$C$_2$ (crb) is the diffusant source. Secondly, the interface concentration of Cr^{2+} increases as fO$_2$ decreases, from around 10 µg/g in air to around 10000 µg/g at fO$_2$ = $10^{-11.1}$ bars. The equilibrium Cr^{2+} concentration is lower in the crb-buffered experiment than its higher fO$_2$ equivalent where mcr is the Cr source.

3.2.3 Valence state changes of diffusing chromium in protoenstatite-buffered experiments

Cr^{2+}/ΣCr is not constant along the diffusion profiles where the fo-prEn-mcr buffer (high aSiO$_2$) is used; a compilation of XANES spectra from all fo-prEn-mcr buffered experiments is shown in Figure 8.

All spectra were then fitted to a linear combination of those of the Cr^{2+} and Cr^{3+} end members; with $Cr^{2+}/\Sigma Cr$ data as a function of distance along fo-prEn-mcr buffered diffusion profiles compiled in Figure 9.

In the experiments conducted between air ($fO_2=10^{-0.7}$ bars) and just below QFM ($fO_2=10^{-7.6}$ bars), $Cr^{2+}/\Sigma Cr$ increases from equilibrium values at the interface to more reduced ratios in the crystal interior. The experiment at $fO_2=10^{-9.6}$ bars (~Fe-FeO equilibria (O'Neill, 1987)), shows no significant $Cr^{2+}/\Sigma Cr$ change along the length of the concentration-distance profile. The experiment at $fO_2 = 10^{-11.1}$ bars shows almost no change along the profile, but with a single point at the tail end possibly representing decreased $Cr^{2+}/\Sigma Cr$. The experiment from the most reducing conditions (C-CO equilibrium) shows no edge shift; the $Cr^{2+}/\Sigma Cr$ ratio stays at around 1 (pure Cr^{2+}) over the length of the profile, although only two points were measured (Figure 4e, Figure 9).

In San Carlos olivine, no change in $Cr^{2+}/\Sigma Cr$ is seen over the length of the diffusion profile, except for the interface spectrum that has the same spectrum as pure Cr^{3+}.

3.2.4   Diffusion of Cr^{3+} - vacancy complexes

With the fo-prEn-mcr buffered Cr profiles resolved into Cr^{2+} and Cr^{3+}, the Cr^{3+} profiles were then fitted using the relationship in eq. (6), where D varies as a function of cation-vacancy binding energy. This was done for all prEn or opx buffered experiments at 1400 °C, except for CODE13 (very low fO_2, essentially no Cr^{3+} present) and CODE16 (experiment was run after XANES spectra were taken). Some fits are shown in Figure 4, with $logD_{Cr3+-[vac]\,pair}$ and G_B values presented in Figure 10 and Table 4. Decreasing fO_2 leads to an increase in the $D_{Cr3+-[vac]\,pair}$ diffusion coefficient and binding energy becoming less negative (weaker binding).

This is associated with the change in diffusion profile shape from near error-function (concave-up) to hockey-stick shaped.

4 Discussion
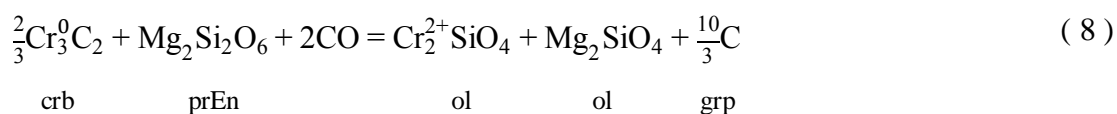
4.1 Cr at the interface

The experiments are designed to achieve the equilibrium concentration of Cr in forsterite at the crystal-buffer interface as controlled by the buffering assemblage. Requirements of internal consistency suggest several ways of validating the assumption of equilibrium, all requiring that the interface concentrations be accurately determined. In addition to testing whether observed concentration gradients really do correspond to lattice diffusion, such measurements are essential where diffusion depends on concentration, and in some cases the measurements can even be used to elucidate equilibrium behaviour that may not otherwise be experimentally accessible.
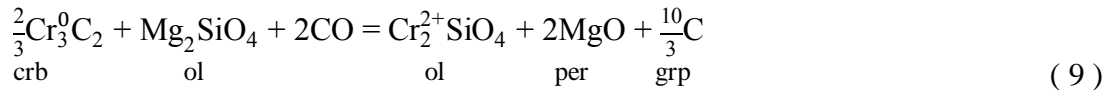
4.1.1 Cr^{2+} incorporation

This is relatively straightforward, as Cr^{2+} replaces Mg^{2+} with no charge imbalance and only minor lattice distortion (ionic radii Cr^{2+}(VI)=0.80 Å, Mg^{2+}(VI)=0.72 Å), forming the $Cr_2^{2+}SiO_4$ substitution, with extensive solid solution along the binary join with Mg_2SiO_4 (Li et al. 1995).

The equilibrium reactions describing substitution of Cr^{2+} as $Cr_2^{2+}SiO_4$ in the two Fe-free assemblages (high and low aSiO$_2$) buffered by chromium carbide, graphite (grp) and carbon monoxide are:

$$\tfrac{2}{3}Cr_3^0C_2 + Mg_2Si_2O_6 + 2CO = Cr_2^{2+}SiO_4 + Mg_2SiO_4 + \tfrac{10}{3}C \qquad (8)$$

$$\quad\text{crb} \qquad\qquad \text{prEn} \qquad\qquad\qquad \text{ol} \qquad\qquad \text{ol} \qquad\qquad \text{grp}$$

and

$$\frac{2}{3}Cr_3^0C_2 + Mg_2SiO_4 + 2CO = Cr_2^{2+}SiO_4 + 2MgO + \frac{10}{3}C$$
crb   ol   ol   per   grp   (9)

Given the low concentrations of Cr^{2+} in these experiments, we may assume that all

components except $Cr_2^{2+}SiO_4$ have activity of one in their relevant phases. Deriving

the equilibrium constant for both reactions, and using the relationship $\ln K = -\Delta G°/(RT)$,

then subtracting the relevant expression for (9) from that for (8), gives:

$$\ln \left(a^{ol}_{Cr_2^{2+}SiO_4} \right)^{fo-prEn-crb} - \ln \left(a^{ol}_{Cr_2^{2+}SiO_4} \right)^{fo-per-crb} = -(\Delta G°(8) - \Delta G°(9))/RT \qquad (10)$$

where superscript fo-prEn-crb refers to the buffering conditions in which the

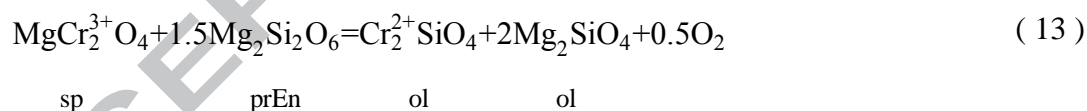relationship is valid, and $\Delta G°(8) - \Delta G°(9)$ refers to the free energy of reaction (11):

$$Mg_2Si_2O_6 + 2MgO = 2Mg_2SiO_4 \qquad (11$$
prEn   per   ol
)

This is described in more detail in Jollands et al. (2014, 2016a). Mixing in olivine on

the $Cr_2^{2+}SiO_4 - Mg_2SiO_4$ binary takes place on two sites per formula unit (two Cr

replace two Mg), therefore $a^{ol}_{Cr_2^{2+}SiO_4} = (\gamma^{ol}_{Cr_2^{2+}SiO_4} X^{ol}_{Cr_2^{2+}SiO_4})^2$ or $a^{ol}_{Cr_2^{2+}SiO_4} \propto (X^{ol}_{Cr_2^{2+}SiO_4})^2$;

i.e. the mole fraction squared is proportional to the activity. Then, assuming that the

activity coefficient, γ, is constant (Henry's law), eq. (10) can be rearranged, with

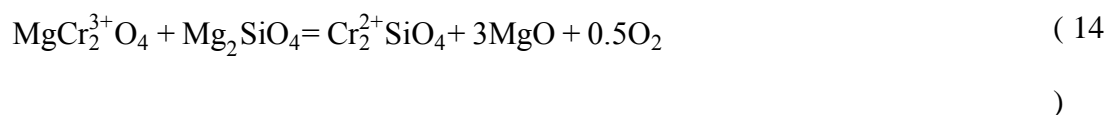mole fraction (i.e. the measurable quantity) substituted in for activity:

$$\frac{\left(X^{ol}_{Cr_2^{2+}SiO_4}\right)^{fo\text{-}prEn\text{-}crb}}{\left(X^{ol}_{Cr_2^{2+}SiO_4}\right)^{fo\text{-}per\text{-}crb}} = \left(\exp\frac{-(\Delta G^o(\,11\,))}{RT}\right)^{\frac{1}{2}} \tag{12}$$

The square root is due to the two-site mixing. Using free energy of formation data from Holland and Powell (2011) to determine the free energy of (11) gives a value of 6.6 at 1400 °C, i.e. 6.6 x more Cr^{2+} at the interface of protoenstatite-buffered experiments than periclase-buffered (line 'Cr^{2+} predicted (crb)' in Figure 11a). The Cr concentrations at the interfaces of protoenstatite and periclase buffered experiments are 2116 µg/g ($\pm$188) and 228 µg/g ($\pm$24) respectively (errors are standard deviations from repeat measurements), giving a ratio of 9.3 ($\pm$1.3), which is slightly higher than predicted.

The equivalent reactions in the two assemblages with magnesiochromite (referring to the lowest fO$_2$ magnesiochromite-buffered experiments) are:

$$MgCr_2^{3+}O_4 + 1.5Mg_2Si_2O_6 = Cr_2^{2+}SiO_4 + 2Mg_2SiO_4 + 0.5O_2 \tag{13}$$

    sp   prEn   ol   ol

and

$$MgCr_2^{3+}O_4 + Mg_2SiO_4 = Cr_2^{2+}SiO_4 + 3MgO + 0.5O_2 \tag{14}$$

    sp   ol   ol   per

Subtraction of (14) from (13) gives:

$$1.5Mg_2Si_2O_6 + 3MgO = 3Mg_2SiO_4 \tag{15}$$
$$\underset{\text{prEn}}{} \quad \underset{\text{per}}{} \quad \underset{\text{ol}}{}$$

In this case, the predicted ratio of the interface concentration (from the thermodynamic database, using a similar treatment as presented above) of Cr^{2+} between the fo-prEn-mcr and fo-per-mcr buffered assemblages is 17.0 at 1400 °C (line 'Cr^{2+} predicted (mcr)' in Figure 11a), a factor of ~2.5 higher than for the fo-prEn-crb and fo-per-crb experiments. This is in good agreement with the ratios derived from the total (i.e. rather than Cr^{2+} or Cr^{3+}) Cr data (Figure 11), but the low fO_2, high $aSiO_2$ experiments buffered with magnesiochromite also contain some (<10%) Cr^{3+}, and the Cr^{3+} concentration in the equivalent low $aSiO_2$ experiment has not been quantified.

4.1.2 Cr^{3+} incorporation

For Cr^{3+}, the equilibria governing the equilibrium concentrations are not as obvious. There is firstly uncertainty as to how Cr^{3+} substitutes into Mg_2SiO_4, which defines the stoichiometry of the appropriate components, and uncertainty as to how this affects the configurational entropy. Cr^{3+} has a strong octahedral site preference, from the crystal field effect (Papike et al., 2005). At high $aSiO_2$ a substitution mechanism forming M-site vacancies is favoured, and in the pure forsterite system with negligible impurities, this is limited to $Cr^{3+}_{4/3}[vac]_{2/3}SiO_4$, where [vac] represents a vacant site. Such a component could alternatively be written $Cr^{3+}_{2/3}[vac]_{1/3}MgSiO_4$ or $Cr^{3+}_2[vac]Mg(SiO_4)_2$ but this makes no difference for present purposes, because the stoichiometry of substitution reactions do not change. As the component is comprised of Cr^{3+} and a vacancy, its configurational entropy depends on the extent of short-range ordering between them.

The evidence from olivine/melt partitioning experiments at high fO$_2$ (where nearly all Cr is trivalent) is that the activity of the Cr^{3+} component is proportional to the Cr concentration, because the partition coefficient does not change with Cr concentration (e.g., Mallmann and O'Neill 2009). Hence $a^{ol}_{Cr^{3+}_{4/3}[vac]_{2/3}SiO_4}$ is proportional to $(X^{ol}_{Cr^{3+}})^{4/3}$ (molar Cr^{3+}/(Cr^{3+}+Mg)). Physically this may be rationalised if pure Cr^{3+} substitutes onto octahedral sites with the positions of the charge balancing vacancies completely specified by the positions of the Cr^{3+}. Note, however, that the olivine/melt partitioning experiments were carried out in systems containing Al$_2$O$_3$ as a major component that would allow the Tschermak's type MgCr^{3+}AlO$_4$ substitution, not available in the present Al-poor situation (nominally Al-free; ~30 μg/g Al in the pure forsterite (Zhukova et al, 2014)).

The reaction describing the stoichiometry of the Al-free substitution from magnesiochromite at high aSiO$_2$ is:

$$\frac{4}{3}Mg_2Si_2O_6 + \frac{2}{3}MgCr^{3+}_2O_4 = Cr^{3+}_{4/3}[vac]_{2/3}SiO_4 + \frac{5}{3}Mg_2SiO_4 \qquad (16)$$
$$\quad\ \text{prEn} \qquad\qquad \text{sp} \qquad\qquad\quad\ \text{ol} \qquad\qquad\quad \text{ol}$$

The equivalent reaction at low aSiO$_2$ would be:

$$Mg_2SiO_4 + \frac{2}{3}MgCr^{3+}_2O_4 = Cr^{3+}_{4/3}[vac]_{2/3}SiO_4 + \frac{8}{3}MgO \qquad (17)$$
$$\text{ol} \qquad\quad\ \text{sp} \qquad\qquad\quad\ \text{ol} \qquad\qquad\quad \text{per}$$

Subtracting eq. (17) from (16) relates the ratio of the activities of the Cr^{3+}-vacancy defect in the prEn-buffered experiments to those in the periclase-buffered experiments through the reaction:

$$\frac{4}{3}Mg_2Si_2O_6 + \frac{8}{3}MgO = \frac{8}{3}Mg_2SiO_4 \qquad (18$$
$$\quad\ \text{prEn} \qquad\quad \text{per} \qquad\quad \text{ol}$$
$$)$$

that predicts $(X^{ol}_{Cr^{3+}})_{prEn}/(X^{ol}_{Cr^{3+}})_{per}$ is 43.8, using a similar treatment as that described above. This value is shown against the data in Figure 11a. The Cr interface concentration in equilibrium with prEn in air (minimal Cr^{2+}) is 1163 ± 44 µg/g, so the predicted concentration in equilibrium with per is 27 ± 1 µg/g, slightly less than the observed 39 ± 1 µg/g. There is, however, the implication from the XANES spectroscopy that the Cr^{3+} substitution into forsterite at the low aSiO$_2$ condition is different to that at the high aSiO$_2$ condition. The remaining ~ 12 µg/g might be assigned to the different substitution mechanism that we suggest to be the spinel-type substitution, $Cr_2^{3+}MgO_4$. The existence of an alternative mode of substitution must enhance the total solubility, as observed, albeit qualitatively.

The concentration of Cr^{3+} as this $Cr_2^{3+}MgO_4$ substitution in equilibrium with $MgCr_2O_4$ (magnesiochromite) is controlled by the reaction:

$$\underset{sp}{MgCr_2^{3+}O_4} = \underset{ol}{Cr_2^{3+}MgO_4} \tag{19}$$

which is notably independent of both fO$_2$ and aSiO$_2$. This means that the small amount of Cr^{3+} in this substitution seen in the per-buffered experiment in air should also be present at the same amount in all experiments with magnesiochromite, but is hidden in the prEn-buffered experiments by the far higher amount of Cr^{3+} occurring as the vacancy-balanced substitution.

4.1.3 The effect of oxygen fugacity

The changing concentrations of Cr^{2+} and Cr^{3+} as a function of fO$_2$ (pure forsterite experiments) gives another level of certainty that the interface concentrations represent equilibrium. The general trend is that the concentration of Cr^{2+} increases as

$f\mathrm{O}_2$ decreases (excluding the chromium carbide-buffered experiment) and the concentration of Cr^{3+} stays the same (Figure 12a).

The substitution reaction of Cr^{3+} from magnesiochromite into forsterite to form the $\mathrm{Cr}^{3+}_{4/3}[\mathrm{vac}]_{2/3}\mathrm{SiO}_4$ component (i.e. reaction (16), above), does not include any free oxygen as no change in oxidation state occurs. Therefore, no $f\mathrm{O}_2$ dependence is predicted from this substitution and indeed, no dependence is observed (Figure 12a). The incorporation of Cr^{2+} into pure forsterite from magnesiochromite liberates oxygen (eqs. (13) and (14), above) hence the Cr^{2+} content of the olivine should increase with decreasing $f\mathrm{O}_2$. The equilibrium constant for reaction (13) can be written:

$$ \mathrm{K} = \frac{\left(a^{\mathrm{prEn}}_{\mathrm{Mg_2Si_2O_6}} \right)^{3/2} a^{\mathrm{sp}}_{\mathrm{MgCr_2O_4}}}{a^{\mathrm{ol}}_{\mathrm{Cr_2SiO_4}} \left(a^{\mathrm{ol}}_{\mathrm{Mg_2SiO_4}} \right)^2 f^{1/2}_{\mathrm{O_2}}} \tag{20} $$

Assuming the activity of forsterite, protoenstatite and magnesiochromite are equal to 1 and the mole fraction of Cr^{2+} is equal to $(a^{\mathrm{ol}}_{\mathrm{Cr_2^{2+}SiO_4}})^2$ (i.e. no short-range order between Cr^{2+} cations, as discussed above), (20) can be reduced to (21):

$$ \mathrm{X}^{\mathrm{ol}}_{\mathrm{Cr}^{2+}} \propto f^{-1/4}_{\mathrm{O_2}} \tag{21} $$

Figure 12a shows the concentration of Cr^{2+} from protoenstatite-buffered experiments as a function of $f\mathrm{O}_2$ fit to the -0.25 exponent with a pre-exponential factor of 16.3 (derived by weighted least-squares regression).

In addition, given that the free energies of formation of all phases in reaction (13) have been measured (Holland and Powell, 2011; Klemme and O'Neill, 1997; Li et al., 1995; Mazandarany and Pehlke, 1974, Holzheid and O'Neill, 1995), the free energy

of the reaction can be calculated using literature data, shown in Supplementary Table 3.

Following Li et al. (1995) eq. (22) is derived from (13):

$$\ln X_{Cr^{2+}}^{ol} = \frac{\frac{1}{2}\Delta G^{o}(\,13\,)-W_{Mg-Cr^{2+}}^{ol}}{RT} + \frac{1}{2}\ln a_{MgCr_2^{3+}O_4}^{sp} + \frac{3}{4}\ln a_{Mg_2Si_2O_6}^{prEn} - \frac{1}{4}\ln f_{O_2} \qquad (\,22\,)$$

where $X_{Cr^{2+}}^{ol}$ is the mole fraction of Cr^{2+} in the olivine phase (defined as molar $Cr^{2+}/(Cr^{2+}+Mg)$), ΔG^{o} (13) is the free energy of reaction (13), $W_{Mg-Cr^{2+}}^{ol}$ is an interaction parameter (8600 J/mol from Li et al. (1995)), $a_{MgCr_2O_4}^{sp}$ is the activity of $MgCr_2O_4$ in the spinel phase and $a_{Mg_2Si_2O_6}^{prEn}$ is the activity of $Mg_2Si_2O_6$ in the protoenstatite phase. Given that these activities are both ≈ 1 (Klemme and O'Neill, 1997), the $\ln a_{Mg_2Si_2O_6}^{prEn}$ and $\ln a_{MgCr_2^{3+}O_4}^{sp}$ terms can be removed. From this relationship, the concentration of Cr^{2+} as a function of $f O_2$ can be calculated, this is shown in Figure 12a along with the measured Cr^{2+} concentration. The data agree well with the prediction from (22) in the middle of the $f O_2$ range, with only minor deviation in the extreme $f O_2$ experiments.

Another independent constraint on the activity-composition relations of the $Cr_{4/3}^{3+}[vac]_{2/3}SiO_4)$, component in olivine is given by the relationship between Cr^{2+} and Cr^{3+} (and with it $Cr^{2+}/\Sigma Cr$) in the fo-prEn-mcr-buffered assemblage and $f O_2$. The equilibrium between the Cr^{2+} and Cr^{3+} substitutions (balanced for one Cr cation) can be written:

$$\frac{1}{2}\underset{ol}{Cr_2^{2+}SiO_4} + \frac{1}{4}\underset{prEn}{Mg_2Si_2O_6} + \frac{1}{4}O_2 = \frac{3}{4}\underset{ol}{Cr_{4/3}^{3+}[vac]_{2/3}SiO_4} + \frac{1}{4}\underset{ol}{Mg_2SiO_4} \qquad (23)$$
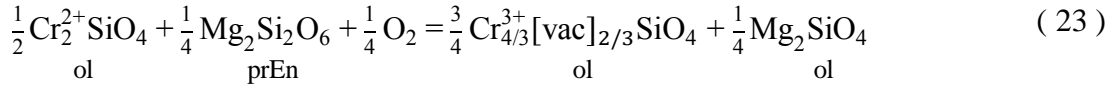
The reaction constant for (23), where a=Xγ (activity equals mole fraction multiplied by activity coefficient), is:

$$K=\frac{\left(X_{Cr_{4/3}^{3+}[vac]_{2/3}SiO_4}^{ol}\gamma_{Cr_{4/3}^{3+}[vac]_{2/3}SiO_4}^{ol}\right)^{3/4}\left(X_{Mg_2SiO_4}^{ol}\gamma_{Mg_2SiO_4}^{ol}\right)^{1/4}}{\left(X_{Cr_2^{2+}SiO_4}^{ol}\gamma_{Cr_2^{2+}SiO_4}^{ol}\right)^{1/2}\left(X_{Mg_2Si_2O_6}^{ol}\gamma_{Mg_2Si_2O_6}^{ol}\right)^{1/4}\left(f_{O_2}\right)^{1/4}} \qquad (24)$$

Assuming that the activities of forsterite and protoenstatite, which are close to unity, cancel out, and that at very low concentrations the activity coefficients are constant (Henry's law) gives:

$$\log\left(\frac{\left(X_{Cr_{4/3}^{3+}[vac]_{2/3}SiO_4}^{ol}\right)^{3/4}}{\left(X_{Cr_2^{2+}SiO_4}^{ol}\right)^{1/2}}\right)=\log\left(\frac{Cr^{3+}}{Cr^{2+}}\right)=\frac{1}{4}\log f_{O_2}+\log K \qquad (25)$$

where K includes the Henry's law activity coefficients. Then with $Cr^{3+}=\Sigma Cr-Cr^{2+}$,

$$\frac{Cr^{2+}}{\Sigma Cr}=\frac{1}{1+10^{\left(\frac{1}{4}\log f_{O_2}+\log K\right)}} \qquad (26)$$

Eq. (26) predicts that the $Cr^{2+}/\Sigma Cr$ ratio (interfaces) follows a sigmoidal relationship as a function of $\log f O_2$, and indeed the data can be fitted to such a curve (Figure 12b). The relationship is almost identical to that found for the AD+Fo melt composition (Berry and O'Neill, 2004), consistent with the observation that the partition coefficients of Cr^{2+} and Cr^{3+} between forsteritic olivine and melt are very similar (Hanson and Jones 1998; Mallmann and O'Neill 2009).

4.2 Chromium diffusion

4.2.1 The effect of aSiO$_2$ on diffusion

A finding in this study, and others, from both our research group and elsewhere, is that minor and trace element diffusion coefficients may be dependent on aSiO$_2$ (e.g. Faak et al., 2013; Jollands et al. 2014, 2016b, 2016c, Zhukova et al., 2014, 2017) This finding has proved contentious, possibly given that many other trace element diffusion studies in the geological literature have not explicitly accounted for this variable, rather experiments have been buffered by, for example, the experimental apparatus or the starting material.

However, whilst it is clear that aSiO$_2$ affects diffusion in a non-negligible way, we do not yet have a unifying explanation for the mechanism by which increasing aSiO$_2$ enhances diffusion of most octahedral site cations in olivine. The first order assumption is that the increased diffusivity must be caused by an increased concentration of octahedral site vacancies in the lattice. Unresolved questions include why the effect of aSiO$_2$ appears to differ for diffusion of cations of different charge: for example, when comparing the results of Zhukova et al. (2014) for Ni^{2+} and Co^{2+} with those of Jollands et al. (2014) for Zr^{4+} and Hf^{4+}, both in pure forsterite. Both of these studies presented observations that the dependence on aSiO$_2$, and thus potentially the diffusion mechanism, changed between pure forsterite and San Carlos olivine. Another issue is how the vacancies are charge balanced. Calculations have suggested that the most stable silica excess defect involves interstitial Si^{4+} cations that each charge-balance two octahedral site vacancies, hence the atomic Mg/Si < 2 (Smyth and Stocker, 1975; Stocker and Smyth, 1978), but changing the Mg/Si of a crystal would require fast diffusion of Si^{4+} into the crystal, which is at odds with experimental studies of Si^{4+} diffusion (Dohmen et al., 2002a). There is also the potential for charge-balance by O vacancies, but this is not in agreement with experimental data, for example, the relationship between aSiO$_2$ and D observed by Zhukova et al. (2014).

4.2.2   Diffusion of Cr^{3+}-vacancy complexes and the effect of Cr^{2+} diffusion

As discussed above, the most likely Cr^{3+} substitution mechanism at high aSiO$_2$ is vacancy-associated, i.e. $Cr^{3+}_{4/3}[vac]_{2/3}SiO_4$, therefore Cr^{3+} diffusion is treated as the diffusivity and binding of Cr^{3+}-vacancy pairs. The potential for a Tschermak's-type $MgCr^{3+}Al^{3+}O_4$ substitution exists, but the alumina content is < 30 µg/g, which is considerably lower than typical Cr^{3+} interface concentrations (~1200 µg/g).

Where the cation and vacancy are strongly bound, the probability of the vacancy exchanging position with the diffusing cation is high. As a result, the mobility of Cr^{3+} is increased, but that of the vacancy is substantially decreased; it is effectively tied to the Cr^{3+}. In this case, an increased concentration of Cr has a lesser effect on the overall effective (i.e. free to move) concentration of metal vacancies, and therefore should have little to no effect on the diffusion of other M-site cations. Where the cation and vacancy are only loosely associated, the vacancy is relatively free to move. This leads to a decreased probability of the charge-balanced Cr^{3+} exchanging positions with a vacancy, but increases the probability of other cations (including other Cr^{3+} ions) in the system swapping with the vacancy. As such, the effective vacancy concentration becomes a function of the Cr^{3+} content, hence a concentration-dependent diffusion regime is established. This affects the shape of the diffusion profiles; concentration-independent diffusion yields error-function shaped profiles, whereas concentration-dependent diffusion profiles tend away from the error function towards hockey stick profiles, depending on the degree of concentration dependence.

Regardless of mechanisms, the data shows that the vacancies are never fully bound to the trivalent Cr. This eliminates the possibility of determining the diffusivity of Cr^{2+} in this system at 'normal' concentrations of octahedral-site vacancies in order to compare with diffusion of other divalent cations (Mg^{2+}, Fe^{2+}, Co^{2+}, Ni^{2+}). When magnesiochromite is present in the buffer; the divalent Cr is diffusing through a matrix where the 'effective' vacancy concentration decreases

away from the crystal edge. This is the reason firstly that Cr^{2+} diffusion profiles only follow the error function in the experiments with negligible Cr^{3+} (the lowest fO_2 experiments, with Cr_3C_2 in the source) and, secondly, the probable reason why Cr^{2+} diffusion in the experiments where Cr^{3+} is present appears much faster than diffusion of other divalent cations.

The shapes of Cr, Cr^{2+} and Cr^{3+} profiles corroborate this - shapes of the Cr^{3+} profiles in protoenstatite-buffered experiments changes from concave-up (near error-function) at high fO_2 (air) to a hockey-stick shapes at low ($10^{-11.1}$ bars) fO_2, which is mirrored by the total Cr, and often the Cr^{2+} diffusion profiles. Therefore, we assume that Cr^{2+} follows the diffusion of Cr^{3+} i.e. Cr^{2+} exploits the vacancies created by Cr^{3+} that are necessary for charge balance. The same behavior was observed by Jollands et al. (2016c) for Ni^{2+}, Co^{2+} and Mn^{2+} diffusion in forsterite in the presence of Ti^{3+} - the trivalent cation enhanced the diffusivity of the divalents. At high fO_2, the associated Cr^{2+} profiles are humped; they show a concentration increase then decrease away from the interface (albeit at very low concentrations), but terminate at the same point as the Cr^{3+} profiles. At more reducing conditions, the Cr^{2+} profiles show a hockey stick shape but at considerably higher concentrations than the Cr^{3+}.

4.2.3 Diffusive anisotropy

Diffusive anisotropy ($D_c \gg D_b > D_a$) in forsterite decreases with decreasing fO_2. Ito and Ganguly (2006) also found diffusive anisotropy ($D_c > D_a$), but only measured it at one fO_2. Spandler and O'Neill (2010) found $D_c > D_a > D_b$ in San Carlos olivine.

The difference in the d-electron configurations of Cr^{2+} and Cr^{3+} in a crystal field, and their ionic radii (0.8 versus 0.63 Å, respectively) are such that they may be expected to occupy different crystallographic sites in olivine. Cr^{2+} is disordered between M1 and M2 (Li et al., 1995), whereas Cr^{3+} is ordered into M1 (Papike et al., 2005). The M1 sites in forsterite form chains with closely spaced (2.98 Å) Mg^{2+} sites along the *c* axis, whereas the distances between M1 sites along the *b*

and *a* axes are 2-3x greater. Therefore, the activation energy for diffusive jumps along *c* is expected to be less than that along the other two axes, if the cation is located predominantly on M1 (as expected for Cr^{3+}).

Spacing between the M2 sites is approximately equal along all three principal axes, between 4.86-5.94 Å. Therefore, it is expected that the diffusive anisotropy of M2 cations should be less than that of those substituting on M1 – this is likely why Ca shows no appreciable anisotropy (Coogan et al, 2005, Spandler and O'Neill, 2010). Cr^{2+} diffusion is somewhere between these two end members in terms of anisotropy – it shows lesser anisotropy than Cr^{3+}, consistent with its distribution over both M1 and M2 (Li et al. 1995). However, despite the similar lack of site preference for Fe^{2+}, the anisotropy is greater than that for Fe-Mg inter-diffusion (e.g. Dohmen and Chakraborty, 2007),

The anisotropy of Cr^{3+} is similar to those of Ni^{2+}, which is known to order markedly into M1 (Boström 1989), and shows similar diffusive anisotropy (Petry et al. 2004; Spandler and O'Neill 2010).

4.2.4 Cr valence state changes along diffusion profiles

$Cr^{2+}/\Sigma Cr$ is not constant along diffusion profiles in pure forsterite, but it is constant in experiments in San Carlos olivine (Figure 8, Figure 9). This suggests that no electronic gradient exists within the San Carlos olivine; it has fully equilibrated with the external fO_2, whereas pure forsterite is unable to equilibrate with the external fO_2 without addition of, in this case, Cr. In San Carlos olivine, electrons should rapidly diffuse into or out of the crystal in response to an imposed fO_2. This will be coupled, in a dry system, with counter-flux of octahedral-site vacancies in order to maintain charge balance. This process should equilibrate a millimeter-sized crystal with the externally controlled fO_2 within a few minutes at 1400 °C (e.g. Demouchy and Mackwell, 2006). The presence of a redox-variable major element (Fe) eliminates the potential

for retention of any intrinsic fO$_2$ in olivine as electronic gradients are rapidly eliminated by fast diffusion.

In pure forsterite, the situation is more complex. When the crystal was grown, the point defects would have been in equilibrium with the fO$_2$ set in the Czochralski furnace, which is controlled by the (unknown) impurities in the inert gas used to protect the crucible from oxidation (e.g. Takei and Kobayashi, 1974). During the diffusion experiment, and in the absence of any redox-variable species already in the crystal, it may not be possible for the point defect structure of the crystal to equilibrate with the externally-buffered fO$_2$, as to do so would require a change in the Mg:Si:O ratios of the crystal. It seems that only when Cr is added is a pathway for electron diffusion created, with the efficiency of equilibration a function of Cr concentration. This may be why, at the tail end of the diffusion profiles, the Cr^{2+}/Cr values all appear to converge.

4.2.5   No effect of pre-annealing on diffusion profiles

One criticism of our experimental protocol is that while considerable care is given to synthesising chemical activity buffer/diffusant source powders, the crystals used as diffusion targets are almost never pre-annealed. There are two main rationales behind pre-annealing in diffusion experiments. The first is related to sample preparation – it has long been observed that when a crystal is polished, the atomic structure in the near surface region (on the order of (tens of) angstroms) becomes mechanically disrupted (Beilby, 1921; Hopkins, 1935), although this has been recently debated (Watson et al., 2016). Thus, crystals are annealed prior to introduction of the diffusant source to return this possibly disrupted region to a crystalline structure. This pre-annealing could be advantageous when the analytical technique used is able to determine concentration changes on the nanoscale, but it has been demonstrated as unnecessary by several authors (Dohmen et al., 2007; Thomas et al., 2008; Watson and Cherniak, 2003), suggesting that the crystal surface is able to recover relatively quickly at the beginning of the diffusion

experiment. Given we do not, when analysing by LA-ICP-MS or EPMA, consider profiles less than several tens of micrometres in length (several thousand times longer than the potential thickness of the disrupted layer), pre-annealing for the purpose of recovering damage is unnecessary in our experiments. There may, however, be other problems associated with recrystallisation of the disrupted layer at the nanoscale, such as formation of new nano-topography (King et al. 2017).

The second stated reason for pre-annealing is to equilibrate the point defects in the crystal with the experimental conditions – in this case the reasoning is more questionable. Measurements of the Mg/Si ratio of other crystals of pure forsterite grown by the Czochralski method have shown that the crystals have atomic Mg/Si > 2, (Ricoult and Kohlstedt, 1985; Takei and Kobayashi, 1974) thus are periclase-buffered or tending that way. In contrast, San Carlos olivine crystals are extracted from peridotite xenoliths (Galer and O'Nions, 1989), so are orthopyroxene-buffered. Therefore, the idea is that pre-annealing should be done to bring the different olivine crystals to the same buffering condition, before the diffusion experiment commences.

If the pre-annealing requires homogenisation via diffusion of Si, as has been assumed, then pre-annealing could never work – D_{Si} is orders of magnitude too slow to alter any point defects in any experimentally accessible times. Using D_{Si} from Dohmen et al. (2002a), pre-annealing at 1500 °C would take between half a million and a million years to homogenise a millimetre-sized crystal. If, conversely, the pre-anneal affects point defects by diffusion of vacancies, then a millimetre sized crystal should equilibrate so rapidly that the point defects should homogenise almost instantly (seconds to hours) during the diffusion experiment (e.g. Demouchy and Mackwell, 2006; Nakamura and Schmalzried, 1984; Wanamaker, 1994). This would effectively eliminate the point defect signature of the pre-anneal. That the latter is true is shown in our dataset by: 1) the pre-anneal series, which demonstrates no effect of different pre-anneals on diffusion profiles; 2) the time series, with steady state behaviour after around one day; 3) the

temperature series, demonstrating Arrhenian behaviour, which would not be expected if the crystals took a long time to equilibrate at the start of diffusion experiments; and 4) the fact that aSiO$_2$ of the buffer clearly affects diffusion profiles, not only here but in studies on other cations diffusing into forsterite (Zhukova et al. 2014, 2017; Jollands et al. 2014, 2016b), which would not be the case if the crystals were able to retain the point defect structure set during their growth.

This does not, however, mean that pre-anneals are never worthwhile. In some cases, the pre-anneal is designed to add a certain minor or trace element to a crystal, which then establishes the point defect population in a way that cannot be quickly modified (e.g. MgO doped with Al^{3+}, Crispin, 2011; forsterite doped with Ti^{3+} and Ti^{4+}, Jollands et al. 2016c). In other cases, the pre-anneal is conducted at much higher temperature than the subsequent diffusion anneal – here the diffusive equilibration of point defects is slower than the time allowed during the diffusion experiment. This is the basis of two-stage hydroxylation (e.g. Bai and Kohlstedt, 1993).

4.2.6   Comparisons with other studies

4.2.6.1   Cr diffusion in olivine

Cr diffusion in pure forsterite has not been previously studied, but studies of experimentally produced Cr diffusion in natural olivine (Ito and Ganguly, 2006; Spandler and O'Neill, 2010) exist.

Ito and Ganguly (2006) formed a diffusion couple between San Carlos olivine and Cr$_2$O$_3$ by depositing a thin layer of the latter by thermal evaporation onto polished, oriented faces of the former. These couples were then annealed at 900 to 1100 °C in gas mixes in the region of fO$_2$–T space around that of the iron-wüstite oxygen buffer, to give diffusion profiles in the hundreds of nanometres range that were analysed using SIMS depth profiling.

The Cr_2O_3 deposited on the crystal surface must interact with the olivine in some way – either it simply acts as a Cr source for diffusion or it could react with the crystal. Because the $aSiO_2$ in the experiments of Ito and Ganguly (2006) was not explicitly controlled, we can only speculate as to what occurred. Assuming that the majority of the Cr substituting into the olivine was divalent in their experiments, Cr^{2+} could dissolve into the olivine forming $Cr_2^{2+}SiO_4$, liberating some ferropericlase, leading to low $aSiO_2$ conditions at the interface:

$$(Mg,Fe)_2SiO_4 + Cr_2^{3+}O_3 = Cr_2^{2+}SiO_4 + 2(Mg,Fe)O + \tfrac{1}{2}O_2 \qquad (27)$$
$$\text{ol} \qquad\quad \text{esk} \qquad\quad \text{ol} \qquad\qquad \text{fpr}$$
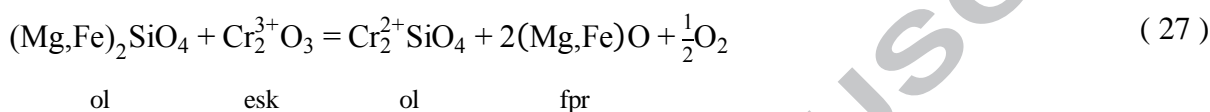
Conversely, the surface of the olivine could react with the Cr_2O_3 to produce orthopyroxene and spinel, hence giving high $aSiO_2$:

$$(Mg,Fe)_2SiO_4 + Cr_2^{3+}O_3 = (Mg,Fe)Cr_2^{3+}O_4 + \tfrac{1}{2}(Mg,Fe)_2Si_2O_6 \qquad (28)$$
$$\text{ol} \qquad\quad \text{esk} \qquad\quad \text{mcr} \qquad\qquad \text{opx}$$
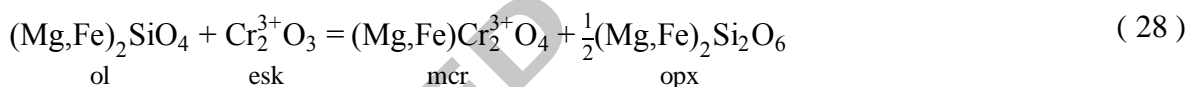
The Ito and Ganguly (2006) Arrhenius relationships extrapolated up temperature gives diffusion coefficients that nearly overlap with our low $aSiO_2$ experiments (Figure 13a), suggesting (27) occurred. With this interpretation, there would be no considerable disagreement between the two studies, but their Mn-Cr closure temperatures would be valid only for systems with low $aSiO_2$. Spandler and O'Neill (2010) presented the diffusion of Cr (along with a cacophony of other elements) in San Carlos olivine at one condition; 1300 °C, 1 atm and fO_2 slightly below QFM. The Cr source was a melt of approximately basaltic composition, for which $aSiO_2$ would be close to, but below, that defined by orthopyroxene-saturation. The $Cr^{2+}/\Sigma Cr$ in the melt should be approximately 0.5 (Figure 12b) Assuming an activation energy for diffusion of 200 kJmol^{-1} in San Carlos olivine (from Dohmen and Chakraborty, 2007), the result of Spandler & O'Neill

(2010) projected to 1400 °C should be logD = -14.2 m²/s, two orders of magnitude faster than the rate given by Ito and Ganguly (2006) but slightly slower than the diffusivities presented in this study (logD = -13.6 to -13.8 m²/s at 100-200 µg/g Cr in San Carlos olivine), which is qualitatively as expected given the difference in aSiO$_2$. The Spandler & O'Neill (2010) experiments were so compositionally complex that it is impossible to determine exactly which charge balance, and hence diffusion, mechanism was responsible for their Cr profiles. In addition, Cr diffused out of their olivine rather than in, as in our experiments, and the difference between out-diffusion versus in-diffusion is poorly understood in this system. Their diffusion profiles followed the error function, indicating no concentration dependence of diffusion; this is unsurprising, as various charge-balancing mechanisms could exist that preclude the necessity for substituting vacancies along with trivalent chromium, notably MgCr^{3+}AlO$_4$.

4.2.6.2 Diffusion of Cr versus other cations in olivine

According to the study of Ito and Ganguly (2006), Cr diffusion in olivine is slower than that of Fe-Mg, the "yard-stick" of diffusion in olivine (see their Fig. 4). We show that this is not always the case, in line with observations from nature (Tollan et al., 2015). We suggest, however, that this is simply because their experiments being conducted at low aSiO$_2$, whereas the comparator experiments of Dohmen et al. (2007) were conducted at high aSiO$_2$, due to the difference in their processes for thin film deposition. The pulsed laser deposition technique (Dohmen et al., 2002b) tends to produce a slight silica excess in thin films when ablating stoichiometric olivine (see Dohmen et al., 2007).

According to our dataset, Cr diffusion in pure forsterite at fO$_2$ corresponding to that of the Fe-FeO buffer, at aSiO$_2$ corresponding to forsterite plus protoenstatite, along the c axis, at Cr contents of 10-500 µg/g is as fast as Fe-Mg inter-diffusion (Figure 13). It is slower than the light elements for which diffusion coefficients have been defined (Li, Be, H) and faster than Ca,

which is likely slowed down by its preference for the widely spaced M2 sites in olivine. Cr diffusion is considerably faster than O and Si diffusion.

However, we urge caution here – experiments are needed where Cr diffusivity is determined in Fe-bearing olivine, at controlled aSiO$_2$, as a function of temperature. Such experiments would be complimentary to those of both Ito and Ganguly (2006) and this study. It is probable that the activation energy for diffusion is lower in Fe-bearing olivine than in pure forsterite (observed for Ni, Ca, Mg), such that extrapolating our diffusion coefficients down-temperature for geospeedometry or closure temperature calculations for natural olivine could induce large errors.

5 Implications

1. The rate of Cr diffusion is similar to Fe-Mg inter-diffusion, when chemical activity is buffered at the same conditions. This may require a re-evaluation of the Mn-Cr closure temperature for high aSiO$_2$ samples.

2. Cr^{3+} in forsterite shows concentration-dependent diffusion. Hence, results from experiments conducted at high Cr concentrations (i.e. this study) cannot be simply extrapolated to natural systems without consideration of this effect.

3. The very near interface region of diffusion experiments can be used to determine equilibrium at conditions where synthesis experiments are not possible, or are more difficult.

4. The assumption of equilibrium at the interface must be satisfied in diffusion experiments. If it cannot be, explanations should be provided as to why not.

5. Predominant substitution mechanisms may change as a function of chemical activities.

References

Akhmetzyanov, D., Dudnikova, V., Zharikov, E., Zhiteitsev, E., Zaitseva, O., Konovalov, A., Tarasov, V. (2013) EPR study of the effect of partial pressure of oxygen in the growth atmosphere on concentration of chromium centers in synthetic forsterite. Physics of the Solid State 55, 520-528.

Bai, Q. and Kohlstedt, D.L. (1993) Effects of chemical environment on the solubility and incorporation mechanism for hydrogen in olivine. Physics and Chemistry of Minerals 19, 460-471.

Beilby, G. (1921) Aggregation and flow of solids. Macmillan. London.

Bell, A.S., Burger, P.V., Le, L., Shearer, C.K., Papike, J.J., Sutton, S.R., Newville, M., Jones, J. (2014) XANES measurements of Cr valence in olivine and their applications to planetary basalts. American Mineralogist 99, 1404-1412.

Berry, A.J., O'Neill, H.S.C., Scott, D.R., Foran, G.J., Shelley, J.M.G. (2006) The effect of composition on Cr^{2+}/Cr^{3+} in silicate melts. American Mineralogist 91, 1901-1908.

Berry, A.J., O'Neill, H.S.C. (2004) A XANES determination of the oxidation state of chromium in silicate glasses. American Mineralogist 89, 790-798.

Boström D. (1989) Cation ordering at 1300 °C in the (Ni, Mg)-olivine solid-solution series. Acta Chemica Scandinavica 43, 116–120.

Brady, J.B., Cherniak, D.J. (2010) Diffusion in minerals: an overview of published experimental diffusion data. Reviews in mineralogy and geochemistry 72, 899-920.

Burns, R.G. (1975) On the occurrence and stability of divalent chromium in olivines included in diamonds. Contributions to Mineralogy and Petrology 51, 213-221.

Chakraborty, S. (2010) Diffusion coefficients in olivine, wadsleyite and ringwoodite. Reviews in mineralogy and geochemistry 72, 603-639.

Coogan, L. A., Hain, A., Stahl, S., Chakraborty, S. (2005). Experimental determination of the diffusion coefficient for calcium in olivine between 900 °C and 1500 °C. Geochimica et Cosmochimica Acta 69, 3683-3694.

Costa, F., Dohmen, R. and Chakraborty, S. (2008) Time scales of magmatic processes from modeling the zoning patterns of crystals. Reviews in Mineralogy and Geochemistry 69, 545-594.

Costa, F., Dungan, M. (2005) Short time scales of magmatic assimilation from diffusion modeling of multiple elements in olivine. Geology 33, 837-840.

Crank, J. (1975). The Mathematics of Diffusion. Oxford, Oxford University Press.

Crispin, K. L. (2011). Cation diffusion in periclase. PhD Thesis, Case Western University.

Demouchy, S. and Mackwell, S. (2006) Mechanisms of hydrogen incorporation and diffusion in iron-bearing olivine. Physics and Chemistry of Minerals 33, 347-355.

Demouchy, S. and Mackwell, S. (2003). Water diffusion in synthetic iron-free forsterite. Physics and Chemistry of Minerals 30, 486-494.

Dodson, M.H. (1973) Closure temperature in cooling geochronological and petrological systems. Contributions to Mineralogy and Petrology 40, 259-274.

Dohmen, R., Becker, H.-W. and Chakraborty, S. (2007) Fe–Mg diffusion in olivine I: experimental determination between 700 and 1,200 °C as a function of composition, crystal orientation and oxygen fugacity. Physics and Chemistry of Minerals 34, 389-407.

Dohmen, R., Chakraborty, S. (2007). Fe–Mg diffusion in olivine II: point defect chemistry, change of diffusion mechanisms and a model for calculation of diffusion coefficients in natural olivine. Physics and Chemistry of Minerals, 34, 409-430.

Dohmen, R., Chakraborty, S. and Becker, H.-W. (2002a) Si and O diffusion in olivine and implications for characterizing plastic flow in the mantle. Geophysical Research Letters 29, 2030.

Dohmen, R., Becker, H. W. Meissner, E. Etzel, T. Chakraborty, S. (2002b). Production of

silicate thin films using pulsed laser deposition (PLD) and applications to studies in mineral

kinetics. European Journal of Mineralogy 14, 1155-1168.

Dohmen, R., Kasemann, S.A., Coogan, L.A., Chakraborty, S. (2010). Diffusion of Li in olivine. Part I: experimental observations and a multi species diffusion model. Geochimica et Cosmochimica Acta 74, 274-292.

Eggins, S.M., Shelley, J.M.G. (2002) Compositional heterogeneity in NIST SRM 610-617 glasses. Geostandards Newsletter 26, 269-286.

Faak, K., Chakraborty, S. and Coogan, L.A. (2013) Mg in plagioclase: Experimental calibration of a new geothermometer and diffusion coefficients. Geochimica Et Cosmochimica Acta 123, 195-217.

Gaetani, G.A., Watson, E.B., (2000). Open system behavior of olivine-hosted melt inclusions. Earth Planet Sc Lett 183, 27-41.

Galer, S.J.G. and O'Nions, R.K. (1989) Chemical and isotopic studies of ultramafic inclusions from the San-Carlos volcanic field, Arizona - a bearing on their petrogenesis. Journal of Petrology 30, 1033-1064.

Ganguly, J., Tirone, M. (1999) Diffusion closure temperature and age of a mineral with arbitrary extent of diffusion: theoretical formulation and applications. Earth and Planetary Science Letters 170, 131-140.

Ganguly, J., Tirone, M. (2001) Relationship between cooling rate and cooling age of a mineral: Theory and applications to meteorites. Meteoritics & Planetary Science 36, 167-175.

Hanson, B., Jones, J.H., 1998. The systematics of Cr^{3+} and Cr^{2+} partitioning between olivine and liquid in the presence of spinel. Am Mineral 83, 669-684.

Hermann, J., O'Neill, H.S.C., Berry, A.J., 2005. Titanium solubility in olivine in the system TiO_2-MgO-SiO_2: no evidence for an ultra-deep origin of Ti-bearing olivine. Contributions to Mineralogy and Petrology 148, 746-760.

Holland, T.J.B., Powell, R. (2011) An improved and extended internally consistent thermodynamic dataset for phases of petrological interest, involving a new equation of state for solids. Journal of Metamorphic Geology 29, 333-383.

Holzheid, A., O'Neill, H.S.C., 1995. The CrO-Cr_2O_3 oxygen buffer and the free energy of formation of Cr_2O_3 from high-temperature electrochemical measurements. Geochimica et Cosmochimica Acta 59, 475-479.

Hopkins, H. (1935) The thickness of the amorphous layer on polished metals. Transactions of the Faraday Society 31, 1095-1101.

Ito, M., Ganguly, J. (2006) Diffusion kinetics of Cr in olivine and ^{53}Mn-^{53}Cr thermochronology of early solar system objects. Geochimica et Cosmochimica Acta 70, 799-809.

Jochum, K.P., Weis, U., Stoll, B., Kuzmin, D., Yang, Q., Raczek, I., Jacob, D.E., Stracke, A., Birbaum, K., Frick, D.A., Günther, D., Enzweiler, J. (2011) Determination of reference values for NIST SRM 610–617 glasses following ISO guidelines. Geostandards and Geoanalytical Research 35, 397-429.

Jollands, M.C., O'Neill, H.St.C., Hermann, J. (2014) The importance of defining chemical potentials, substitution mechanisms and solubility in trace element diffusion studies: the case of Zr and Hf in olivine. Contributions to Mineralolgy and Petrology 168, 1-19.

Jollands, M.C., Burnham, A.D., O'Neill, H.S.C., Hermann, J. and Qian, Q. (2016a) Beryllium diffusion in olivine: A new tool to investigate timescales of magmatic processes. Earth and Planetary Science Letters 450, 71-82.

Jollands, M.C., Hermann, J., O'Neill, H.S.C., Spandler, C. and Padrón-Navarta, J.A. (2016b) Diffusion of Ti and some divalent cations in olivine as a function of temperature, oxygen fugacity, chemical potentials and crystal orientation. Journal of Petrology 57, 1983-2010.

Jollands, M.C., Padrón-Navarta, J.A., Hermann, J. and O'Neill, H.S.C. (2016c) Hydrogen diffusion in Ti-doped forsterite and the preservation of metastable point defects. American Mineralogist 101, 1560-1570.

Karato, S.I. (1990) The role of hydrogen in the electrical conductivity of the upper mantle. Nature 347, 272-273.

Keith, M.L. (1954) Phase equilibria in the system $MgO-Cr_2O_3-SiO_2$. Journal of the American Ceramic Society 37, 490-496.

King, H. E., Plümper, O., Putnis, C. V., O'Neill, H. S. C., Klemme, S., & Putnis, A. (2017). Mineral surface rearrangement at high temperatures: Implications for extraterrestrial mineral grain reactivity. ACS Earth and Space Chemistry, 1, 113-121.

Klemme, S., O'Neill, H.S.C. (1997) The reaction $MgCr_2O_4 + SiO_2 = Cr_2O_3 + MgSiO_3$ and the free energy of formation of magnesiochromite ($MgCr_2O_4$). Contributions to Mineralogy and Petrology 130, 59-65.

Li, J.-P., O'Neill, H.S.C., Seifert, F. (1995) Subsolidus phase relations in the system $MgO-SiO_2-Cr-O$ in equilibrium with metallic Cr, and their significance for the petrochemistry of chromium. Journal of Petrology 36, 107-132.

Lugmair, G.W., Shukolyukov, A. (1998) Early solar system timescales according to $^{53}Mn-^{53}Cr$ systematics. Geochimica et Cosmochimica Acta 62, 2863-2886.

Mallmann, G., O'Neill, H.S.C. (2009) The crystal/melt partitioning of V during mantle melting as a function of oxygen fugacity compared with some other rlements (Al, P, Ca, Sc, Ti, Cr, Fe, Ga, Y, Zr and Nb). Journal of Petrology 50, 1765-1794.

Mazandarany, F.N., Pehlke, R.D. (1974) Standard free energy of formation of Cr_2O_3. Journal of the Electrochemical Society 121, 711-714.

McKeown, D.A., Buechele, A.C., Tappero, R., McCoy, T.J., Gardner-Vandy, K.G. (2014) X-ray absorption characterization of Cr in forsterite within the MacAlpine Hills 88136 EL3 chondritic meteorite. American Mineralogist 99, 190-197.

Nakamura, A. and Schmalzried, H. (1984) On the Fe^{2+} –Mg^{2+}-interdiffusion in olivine (II). Berichte der Bunsengesellschaft für physikalische Chemie 88, 140-145.

O'Neill, H.S.C. and Pownceby, M.I. (1993) Thermodynamic data from redox reactions at high-temperatures .1. An experimental and theoretical assessment of the electrochemical method using stabilized zirconia electrolytes, with revised values for the Fe- FeO, Co-CoO, Ni-NiO and Cu-Cu_2O oxygen buffers, and new data for the W-WO_2 buffer. Contributions to Mineralogy and Petrology 114, 296-314.

O'Neill, H.S.C. (1987) Quartz-fayalite-iron and quartz-fayalite-magnetite equilibria and the free energy of formation of fayalite (Fe_2SiO_4) and magnetite (Fe_3O_4). American Mineralogist 72, 67-75.

O'Neill, H.S.C., Berry, A.J. (2006) Activity coefficients at low dilution of CrO, NiO and CoO in melts in the system CaO,MgO,Al_2O_3,SiO_2 at 1400 °C: Using the thermodynamic behaviour of transition metal oxides in silicate melts to probe their structure. Chemical Geology 231, 77-89.

Odake, S., Fukura, S., Arakawa, M., Ohta, A., Harte, B., Kagi, H. (2008) Divalent chromium in ferropericlase inclusions in lower-mantle diamonds revealed by micro-XANES measurements. Journal of Mineralogical and Petrological Sciences 103, 350-353.

Pantelouris, A., Modrow, H., Pantelouris, M., Hormes, J., Reinen, D., 2004. The influence of coordination geometry and valency on the K-edge absorption near edge spectra of selected chromium compounds. Chemical physics 300, 13-22.

Papike, J., Karner, J. and Shearer, C. (2005) Comparative planetary mineralogy: Valence state partitioning of Cr, Fe, Ti, and V among crystallographic sites in olivine, pyroxene, and spinel from planetary basalts. American Mineralogist 90, 277-290.

Paton, C., Hellstrom, J., Paul, B., Woodhead, J., Hergt, J. (2011) Iolite: Freeware for the visualisation and processing of mass spectrometric data. Journal of Analytical Atomic Spectrometry 26, 2508-2518.

Peslier, A.H., Bizimis, M., Matney, M., 2015. Water disequilibrium in olivines from Hawaiian peridotites: Recent metasomatism, H diffusion and magma ascent rates. Geochim Cosmochim Ac 154, 98-117.

Petry C., Chakraborty S., Palme H. (2004) Experimental determination of Ni diffusion coefficients in olivine and their dependence on temperature, composition, oxygen fugacity, and crystallographic orientation. Geochimica Cosmochimica Acta 68, 4179–4188.

Rager, H., Taran, M., Khomenko, V., (1991) Polarized optical absorption spectra of synthetic chromium doped Mg_2SiO_4 (forsterite). Physics and Chemistry of Minerals 18, 37-39.

Ricoult, D.L., Kohlstedt, D.L. (1985) Experimental evidence for the effect of chemical environment on the creep rate of olivine. Point Defects in Minerals, 171-184.

Robie, R.A., Hemingway, B.S. (1995) Thermodynamic properties of minerals and related substances at 298.15 K and 1 bar (10^5 Pascals) pressure and at higher temperatures. US Geological Survey Bulletin 2131, 1-461.

Ruprecht, P., Plank, T. (2013) Feeding andesitic eruptions with a high-speed connection from the mantle. Nature 500, 68-72.

Schreiber, H.D., Haskin, L.A., 1976. Chromium in basalts: Experimental determination of redox states and partitioning among synthetic silicate phases, Lunar and Planetary Science Conference Proceedings, pp. 1221-1259.

Smyth, D.M. and Stocker, R.L. (1975) Point defects and non-stoichiometry in forsterite. Physics of the Earth and Planetary Interiors 10, 183-192.

Spandler, C., O'Neill, H.S.C. (2010) Diffusion and partition coefficients of minor and trace elements in San Carlos olivine at 1,300°C with some geochemical implications. Contributions to Mineralogy and Petrology 159, 791-818.

Spandler, C., O'Neill, H.S.C., Kamenetsky, V.S. (2007) Survival times of anomalous melt inclusions from element diffusion in olivine and chromite. Nature 447, 303-306.

Stocker, R. and Smyth, D. (1978) Effect of enstatite activity and oxygen partial pressure on the point-defect chemistry of olivine. Physics of the Earth and Planetary Interiors 16, 145-156.

Sutton, S.R., Jones, K.W., Gordon, B., Rivers, M.L., Bajt, S., Smith, J.V. (1993) Reduced chromium in olivine grains from lunar basalt 15555 - X-Ray absorption near edge structure (XANES). Geochimica et Cosmochimica Acta 57, 461-468.

Takei, H. and Kobayashi, T. (1974) Growth and properties of Mg_2SiO_4 single crystals. Journal of Crystal Growth 23, 121-124.

Thomas, J., Cherniak, D. and Watson, E. (2008) Lattice diffusion and solubility of argon in forsterite, enstatite, quartz and corundum. Chemical Geology 253, 1-22.

Tirone, M., Ganguly, J., Dohmen, R., Langenhorst, F., Hervig, R., Becker, H.-W. (2005). Rare earth diffusion kinetics in garnet: experimental studies and applications. Geochimica et Cosmochimica Acta 69, 2385-2398.

Tollan, P., O'Neill, H.S.C., Hermann, J., Benedictus, A., Arculus, R., 2015. Frozen melt–rock reaction in a peridotite xenolith from sub-arc mantle recorded by diffusion of trace elements and water in olivine. Earth and Planetary Science Letters 422, 169-181.

Ulianov, A., Müntener, O., Schaltegger, U., Bussy, F. (2016). Detection in LA-ICPMS: construction and performance evaluation of decision rules. Journal of Analytical Atomic Spectrometry 31, 597-630.

Van Orman, J.A., Li, C., Crispin, K.L. (2009) Aluminum diffusion and Al-vacancy association in periclase. Physics of the Earth and Planetary Interiors 172, 34-42.

Venkatraman, M., & Neumann, J. P. (1990). The C-Cr (carbon-chromium) system. Bulletin of Alloy Phase Diagrams 11, 152-159.

Wanamaker, B.J. (1994) Point defect diffusivites in San Carlos olivine derived from reequilibration of electrical conductivity following changes in oxygen fugacity. Geophysical Research Letters 21, 21-24.

Watson, E.B. and Cherniak, D.J. (2003) Lattice diffusion of Ar in quartz, with constraints on Ar solubility and evidence of nanopores. Geochimica Et Cosmochimica Acta 67, 2043-2062.

Yen, W., Jia, W. (1995) Advances in the spectroscopy of Cr^{4+}-doped laser materials. Journal of Applied Spectroscopy 62, 966-978.

Watson, E.B., Cherniak, D.J., Thomas, J.B., Hanchar, J.M., Wirth, R. (2016). Crystal surface integrity and diffusion measurements on Earth and planetary materials. Earth and Planetary Science Letters 450, 346-354.

Zhukova, I., O'Neill, H.S.C, Cambell, I.H. and Kilburn, M.R. (2014) The effect of silica activity on the diffusion of Ni and Co in olivine. Contributions to Mineralogy and Petrology 168, 1-15.

Zhukova, I., O'Neill, H.S.C, Campbell, I.H. (2017). A subsidiary fast-diffusing substitution mechanism of Al in forsterite investigated using diffusion experiments under controlled thermodynamic conditions. Contributions to Mineralogy and Petrology, 172, 53.

Figure Captions

Figure 1: Cr Kα X-ray map of the diffusion region recorded from experiment CODE10, *c* axis, fo-prEn-mcr buffer. 2x1 mm, 5 µm step size, 60 ms dwell time. Dark green = high Cr (1764±36 µg/g at crystal edge), white = low Cr (<1 µg/g in the interior of the crystal). The *c* axis is slightly off parallel to *y* in this view. Some Cr diffusion is observed from the adjacent (right side) face of the crystal due to vapour-transport of Cr, but this is would not impinge on the measured diffusion profiles (see typical size of a laser track) unless these were taken unnecessarily close to this edge.

Figure 2: Setup of XANES spectroscopy analyses of diffusion profiles; a cartoon and a photomicrograph showing optical fluorescence, which conveniently assists in locating analytical points. The angle of incidence of the beam is 45° to the sample surface (the surface of the crystal in an epoxy mount) in a plane parallel to the diffusion interface (001), to which the *c* axis ([001] direction) is perpendicular. The detector (also in a plane parallel to (001)) measures those

secondary X-rays that are 90° to the angle of incidence. The incident X-rays are exponentially attenuated in the sample, thus acquired XANES spectra are predominantly derived from the near surface, with only minor contribution from deeper (on the order of tens of microns) inside the crystal.

Figure 3: Interface Cr concentrations. The circles represent experiments conducted in pure forsterite, and stars for those in San Carlos olivine. (a) Cr concentration at the crystal-buffer interface (extrapolated using curve fitting) in both protoenstatite and periclase-buffered conditions as a function of log fO$_2$. (b) As (a), but as a function of inverse temperature at fO$_2 \approx$ Fe-FeO.

Figure 4: Some example diffusion profiles, with experimental parameters, showing total Cr (light grey circles), Cr^{3+} (dark grey circles) and Cr^{2+} (squares). All Cr profiles are fitted to either eq. (2) or (3) (dashed lines), and Cr^{3+} profiles are fitted using the relationship in (6) (solid lines). Fit parameters are given, for errors see Table 2 and Table 3 (a) Oxidised (fO$_2$=10$^{-3.1}$ bars) experiment in forsterite, with concave-up profile. (b) San Carlos olivine experiment conducted at moderate fO$_2$. (c) A reduced (fO$_2$=10$^{-9.6}$ bars) forsterite experiment, showing a hockey stick shaped Cr^{3+} profile and Cr^{2+} at much higher concentrations with the same profile geometry. (d) Profiles from the same experiment as (c), but fo-per-mcr buffered rather than fo-prEn-mcr. Note the much shorter profile and lower interface concentration. (e) A very reduced experiment conducted at fO$_2$ corresponding to the C-CO buffer (fO$_2$=10$^{-16.1}$ bars), showing an error function-shaped Cr profile, comprised of only Cr^{2+} (Cr^{3+} below detection limit). (f) Profile from the 1200 ºC experiment, conducted at approximately the same fO$_2$ ($\approx$ Fe-FeO) as those in (c) and (d).

Figure 5: The effect of experimental fO_2 on Cr diffusion. (a) The recovered diffusion coefficient (fo-prEn-mcr or ol-opx-sp buffered, c axis, 1400 ℃ experiments) as a function of Cr concentration at different experimental fO_2s. The lines are the averages of fits of 3-5 profiles, the grey areas are one standard deviation. (b) Diffusion coefficients as a function of fO_2, at different Cr concentrations (i.e. the same data as (a), recast).

Figure 6: Cr diffusion, along the c axis, as a function of temperature, at various Cr concentrations, and at high (fo-prEn-mcr) and low (fo-per-mcr) $aSiO_2$. Also shown are the data of Ito and Ganguly (2006), extrapolated up temperature using the Tirone et al. (2005) method of calculating error envelopes. The activation energies and pre-exponential factors for these Arrhenius curves (and more) are presented in

Supplementary Table 2.

Figure 7: (a) The end member spectra from c axis experiments. Most spectra can be fit to a linear combination of the $Cr_2^{2+}SiO_4$ and $Cr_{4/3}^{3+}[vac]_{2/3}SiO_4$ end members; the $Cr_2^{3+}MgO_4$ end member is only used in high fO_2, low $aSiO_2$ experiments. Inset: Cr^{2+} and Cr^{3+} (in silicate melt) and spinel standards from Berry and O'Neill (2004). (b) XANES spectra representing the closest measurement to the crystal-buffer interface, for each experimental fO_2, in protoenstatite buffered experiments, at 1400 ℃.

Figure 8: Stacked XANES spectra recorded from all protoenstatite-buffered c axis diffusion experiment (arbitrary offset). The numbers represent the experimental $\log fO_2$ at 1400 °C. For clarity, less than half of the recorded spectra are presented. In all experiments conducted at $fO_2 > 10^{-7.6}$ bars (excluding the experiment in natural olivine, fo_{90}), the interface is more oxidised (higher energy edge) than the interior end of the diffusion profile. The more reduced experiments

show little change between the interface and crystal interior, hence fewer spectra are presented than for the high fO$_2$ experiments. The dashed lines correspond to the two peak positions.

Figure 9: Changes in Cr^{2+}/ΣCr along diffusion profiles from all protoenstatite-buffered experiments in both forsterite (circles) and San Carlos olivine (stars). The numbers represent the log fO$_2$ at 1400 °C of each experiment. The x axis is normalised distance along diffusion profiles calculated as distance (m) divided by square root of time (s). Cr^{2+}/ΣCr from all forsterite experiments appears to converge on the same value at the tail end of diffusion profiles, whereas those from the San Carlos olivine experiment is approximately constant along the profile.

Figure 10: (a) Diffusion coefficients and (b) binding energy of Cr^{3+}-vacancy pairs, in fo-prEn-mcr or ol-opx-sp buffered experiments at 1400 ºC, as a function of experimental fO$_2$. The circles are experiments conducted in Fo$_{100}$, the stars are experiments in Fo$_{90}$ (San Carlos olivine). The diffusion coefficient of the Cr^{3+} vacancy pair increases as the experimental fO$_2$ decreases, and the binding energy between the Cr^{3+} and vacancy becomes less negative.

Figure 11: (a) The ratio between interface Cr concentrations in the two buffering conditions, at 1400 ºC as a function of fO$_2$. Dashed lines represent Cr(prEn)/Cr(per) ratios for pure Cr^{2+} (with both magnesiochromite and chromium carbide as a source) and Cr^{3+}, predicted from thermodynamic data (see discussion). (b) as (a), but as a function of inverse temperature, for the experiments conducted at around Fe-FeO, where most Cr should be Cr^{2+}.

Figure 12: (a) The concentrations of Cr^{2+} and Cr^{3+} at the crystal-buffer interfaces in fo-prEn-mcr buffered experiments, in forsterite, as a function of fO$_2$. The Cr^{3+} concentration stays constant, as expected; no O$_2$ is involved when transferring Cr^{3+} from $MgCr_2^{3+}O_4$ (buffer) to $Cr_{4/3}^{3+}[vac]_{2/3}SiO_4$

(crystal). Cr^{2+} predicted' is calculated using eq. (22). (b) The $Cr^{2+}/\Sigma Cr$ ratio as a function of fO_2, fitted to eq. (26). Also shown is $Cr^{2+}/\Sigma Cr$ from a melt at 1400 °C with forsterite on the liquidus (AD+Fo of (Berry and O'Neill, 2004)), that suggests no change in $Cr^{2+}/\Sigma Cr$ during olivine-melt partitioning. The fO_2 of QFM is calculated from O'Neill (1987).

Figure 13: Cr diffusion coefficients (c axis, $fO_2 \approx$ Fe-FeO) along with those of some other ions in olivine. Faster H: Jollands et al. (2016c), slightly slower H: Demouchy and Mackwell (2003). Be: Jollands et al. (2016a). Li: Dohmen et al. (2010). Fe-Mg: Dohmen et al. (2007). Ca: Coogan et al. (2005). O and Si: Dohmen et al. (2002a). The star represents D_{Cr} along the c axis in San Carlos olivine (Spandler and O'Neill, 2010).

Table Captions

Table 1: Abbreviations of phases and components.

Table 2: Experimental results for high $aSiO_2$ experiments, i.e. buffered by fo-prEn-mcr, fo-prEn-crb or ol-opx-sp. *=San Carlos olivine experiment. The diffusion coefficients are all in m^2/s. $LogD_{Cr}$ at a given concentration, up to the interface concentration, can be extracted from the fitting parameters presented using eq. (5). The interface Cr content is a fitting parameter - it is an extrapolation to the interface from the nearest LA-ICP-MS point (always assumed to be 3 μm from the interface, given that the beam is 6 μm wide). See Supplementary Table 1 for experimental conditions for the fO_2 and T series. n.e. = no experiment conducted, n.a. = not applicable, because D is not concentration dependent within the resolution of our profiles, so $logD=logD_{max}$ regardless of Cr concentration. Errors are 1σ derived from fits to usually five measured profiles.

Table 3: Experimental results for periclase buffered experiments, i.e. buffered by fo-per-mcr, fo-per-crb or ol-fpr-sp. All abbreviations, heading etc. are as in Table 2, except n.r. = not recovered – the diffusion profiles were not long enough to measure using our LA-ICP-MS method.

Table 4: The interface concentrations and diffusion coefficients from XANES spectroscopy, for fo-prEn-mcr or ol-opx-sp buffered experiments at 1400 °C only. The XANES spectroscopy interface measurements were taken 5-10 µm away from the true interface, whereas the LA-ICP-MS interface concentrations were extrapolated to the interface by curve fitting. *experiment in San Carlos olivine, where the interface spectrum showed pure Cr^{3+}, not consistent with the apparently well equilibrated rest of the crystal.

Supplement captions

Supplementary Figure 1: A single diffusion profile (CODE3, *b* axis) measured using both LA-ICP-MS (grey) and EPMA (black). The two techniques show nearly perfect agreement. Inset: EPMA vs LA-ICP-MS, including 1:1 line. The discrepancy between Cr determined by the two methods increases at higher Cr concentration - this is due to increased scatter in the LA-ICP-MS data as the Cr concentration moves away from the ~400 µg/g Cr in NIST SRM 610 (primary standard).

Supplementary Figure 2: Diffusive anisotropy. *c*- and *a*-axis profiles extracted from both high (a) and low (b) fO_2 experiments. The anisotropy decreases (*c*- and *a*- axis profiles are less different) as the fO_2 decreases.

Supplementary Figure 3: The effect of the crystallographic orientation on XANES spectra recorded from a single experiment (CODE10; $fO_2=10^{-5.8}$ bars). The three spectra were recorded

parallel to each of the three principal faces, for example, in the spectra labelled //(001), the beam enters and leaves the sample in a plane parallel to the (001) face – in this case diffusion was being investigated along the c axis. The difference between //(001) and //(010) is minimal – it may relate simply to the analyses being recorded at relatively different points on the diffusion profiles. However, the major difference between these two and the //(100) spectrum precludes the possibility of using bulk spectra of Cr-bearing powders as standards.

Supplementary Figure 4: Examples of Cr diffusion profiles from San Carlos olivine (light grey) and pure forsterite (dark grey) from experiments with comparable fO_2 ($10^{-6.7}$ and $10^{-6.8}$ bars) and the same crystallographic orientation (c axis). The profiles are normalised to the square root of experimental duration. The background Cr concentration in the San Carlos olivine is 135 ± 5 µg/g, and is < 1 µg/g in the pure forsterite. Inset: $logD_{Cr}$ as a function of Cr concentration for both San Carlos olivine and pure forsterite.

Supplementary Figure 5: Results from the time series experiments. (a) Cr diffusion profiles normalised to the square root of experimental duration, offset in 500 µg/g steps for clarity. (b) The Cr diffusion coefficient as a function of experimental duration for three Cr contents, including 2σ uncertainties (derived from 5 measurements on each crystal). The diffusion coefficients appear to stabilise after the 3 day experiment.

Supplementary Figure 6: (a) Cr diffusion profiles (fo-prEn-mcr, b axis, 1400 °C, CO_2, pure forsterite, 7 days) in crystals with different pre-anneal histories, offset in 300 µg/g steps for clarity. There is no discernible difference between the profiles. Model fits are also shown as solid black lines. (b) Extracted Cr diffusion coefficients from different Cr concentrations along

profiles, with error bars representing 2σ, derived from 5 repeat measurements of each crystal. Point colours correspond to those in (a).

Supplementary Figure 7: Results from the buffer composition series. The four experiments were run with different composition buffers in the same three-phase field (inset), and all give indistinguishable diffusion profiles (offset by ~750 µg/g for clarity). See Supplementary Table 1 for experimental conditions. The profile shades in greyscale represent the buffer compositions – they are associated with those of the dots in the inset.

Supplementary Table 1: The experimental conditions. The oxygen fugacity (fO_2) series was conducted at ~1400 °C. CODE5 has an asterisk, as it also belongs to both the time and temperature series. The temperature (T) series was done at fO_2 corresponding to the ~Fe-FeO equilibrium. t is the time series, P-A is the pre-anneal series and Buffer is the buffer composition series. $\log fO_2$ (QFM) and (IW) are the log oxygen fugacity values relative to the SiO_2-Fe_2SiO_4-Fe_3O_4 and Fe-FeO equilibria, from O'Neill (1987) and O'Neill and Pownceby (1993), respectively. t(s) is the experimental duration in seconds, and t(d) is the duration in days (approximate). n is the number of crystals in each run, and dots represent the orientation (//a, //b or //c axes) and buffer composition conditions used (per = fo-per-mcr, prEn = fo-prEn-mcr, or their low fO_2 or Fe-bearing equivalents. fo_{100} is pure forsterite, fo_{90} is San Carlos olivine.

Supplementary Table 2: The Arrhenius parameters for c axis diffusion coefficients at some different Cr concentrations. Errors are 1 standard deviation.
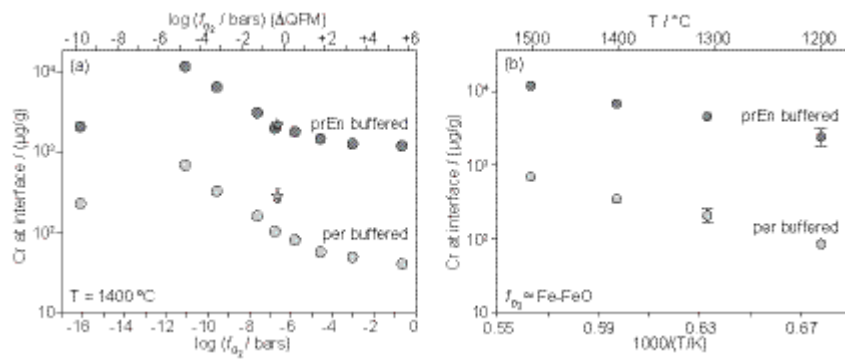
Supplementary Table 3: Thermodynamic data used in this study (at 1400 °C). * ($\Delta_f H°298$ and $S°298$ from K&O'N(97), a, b, c, d (C_p data) from R&H(95)).
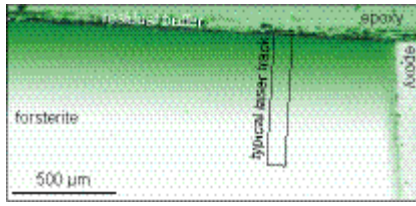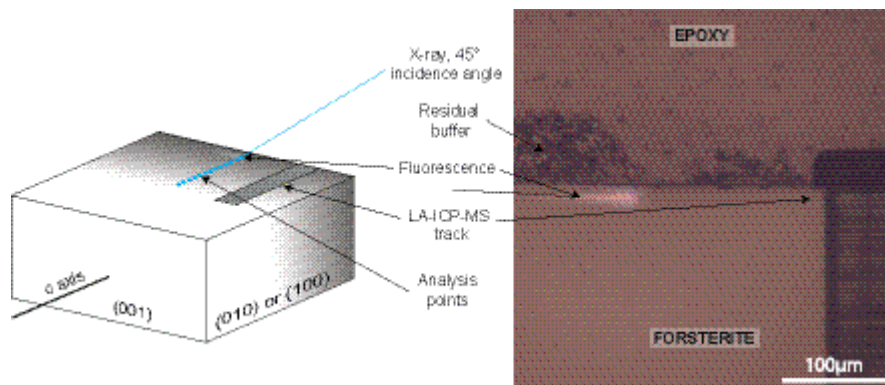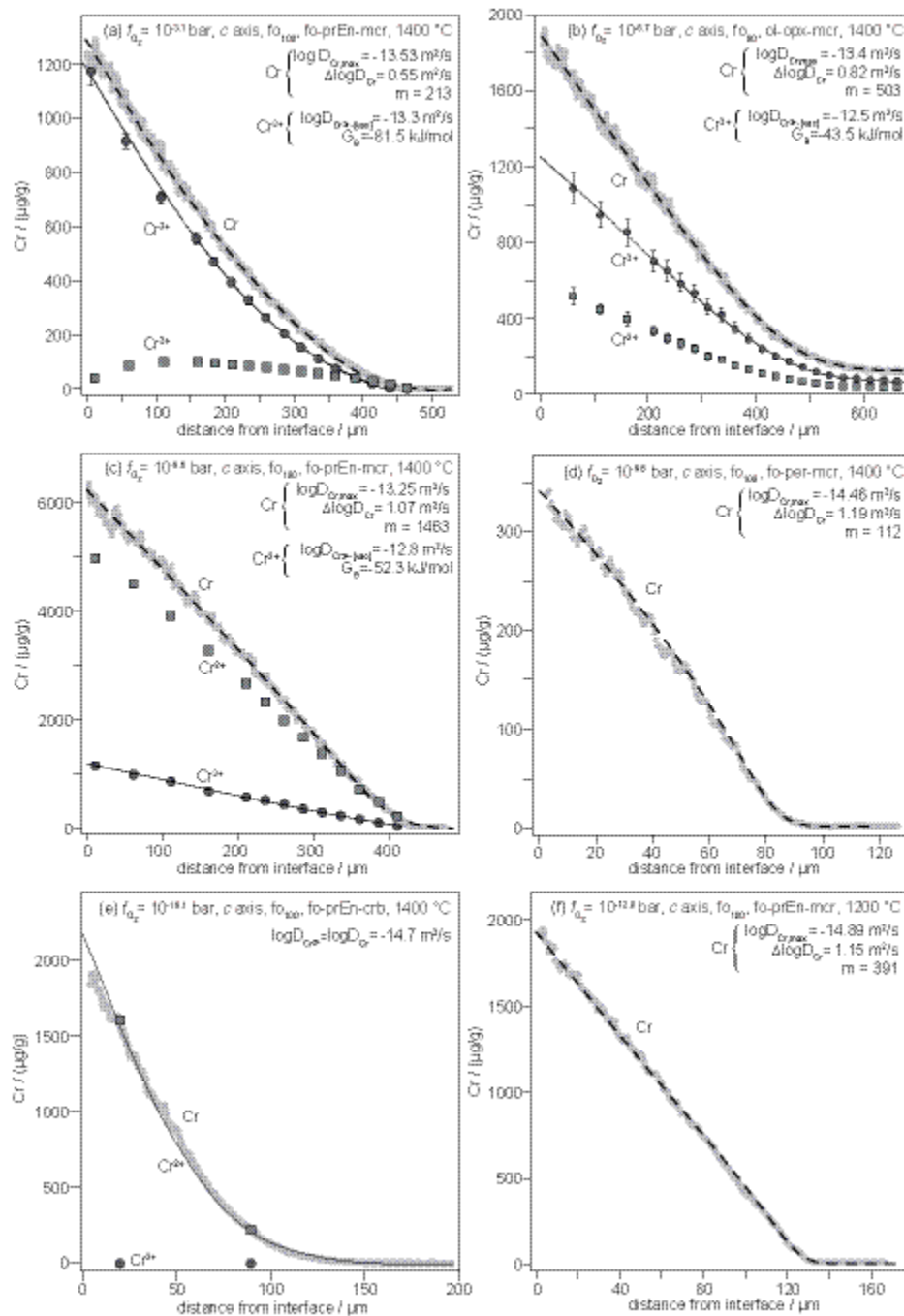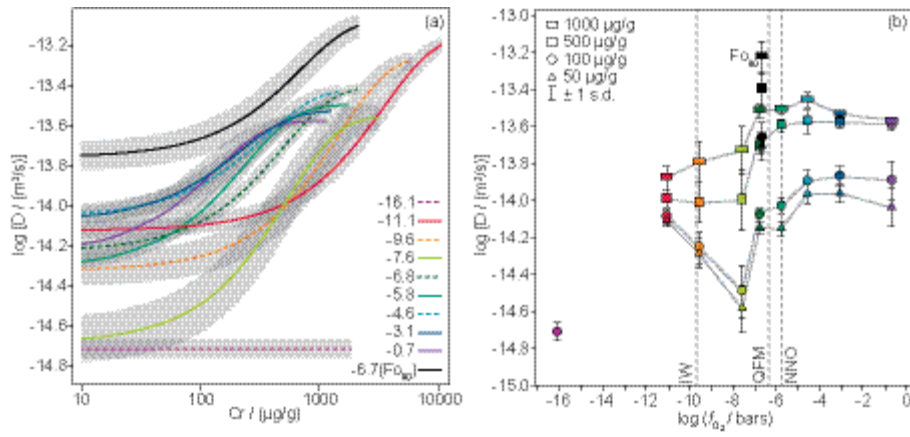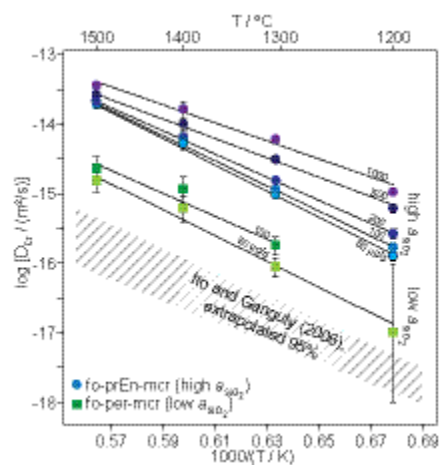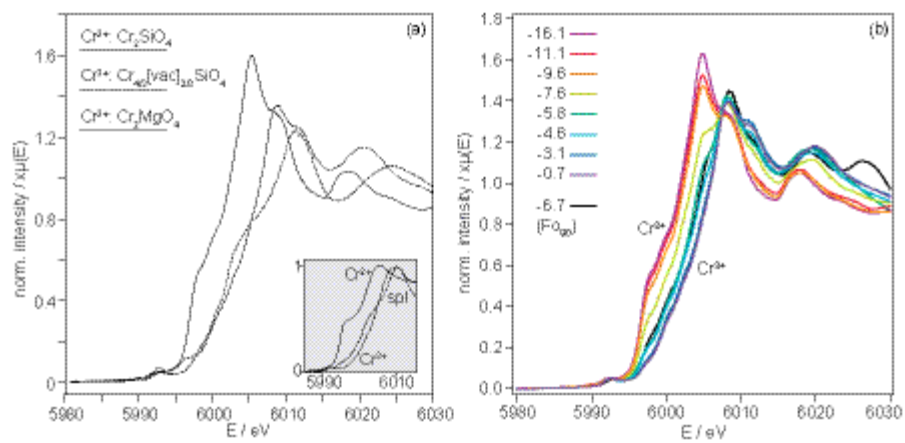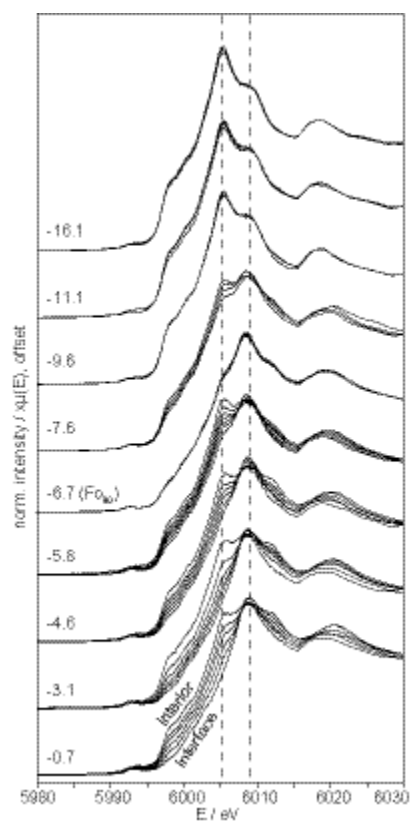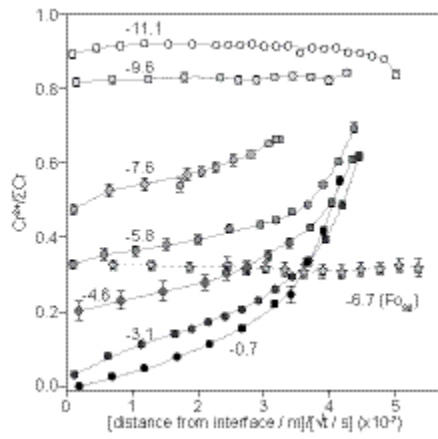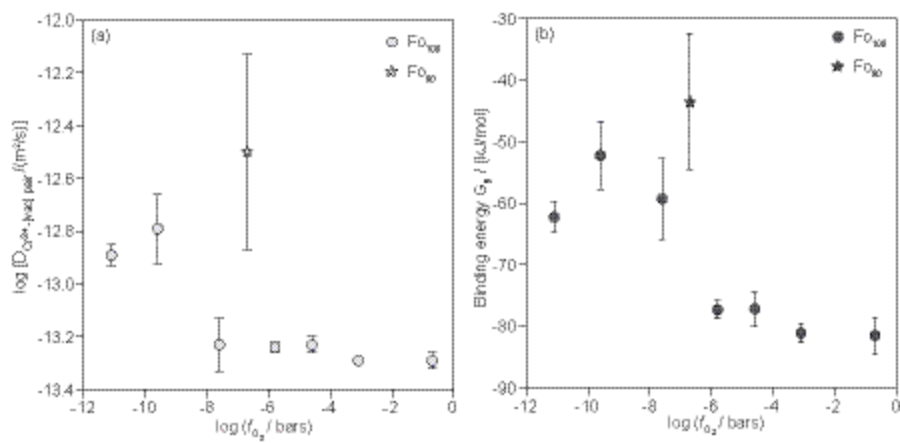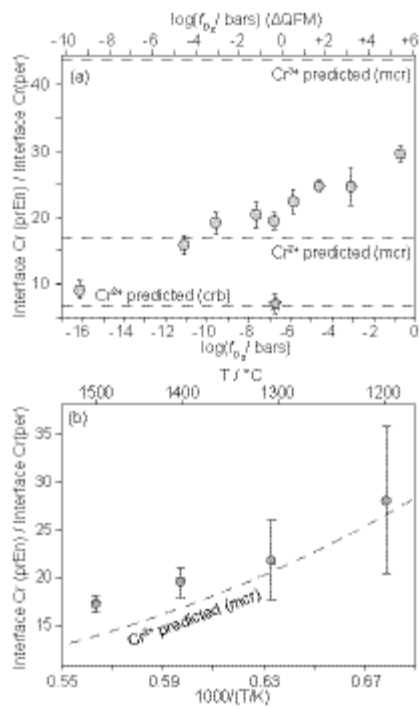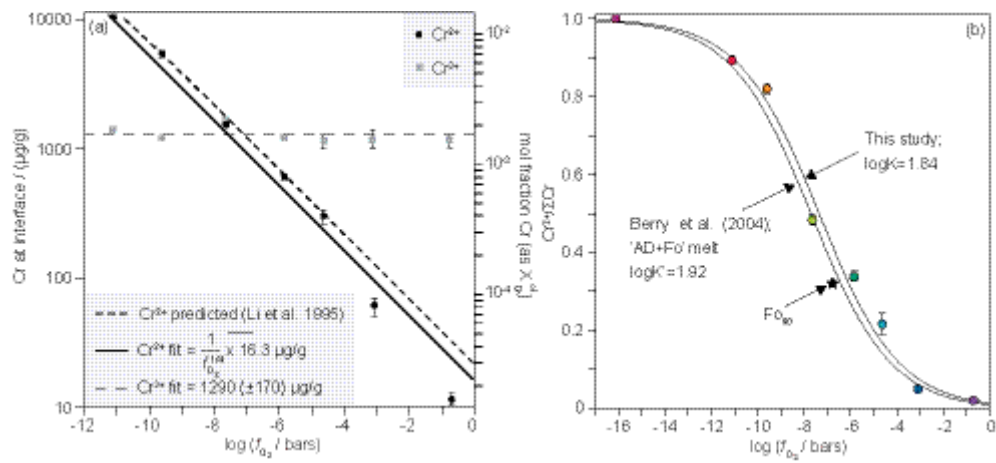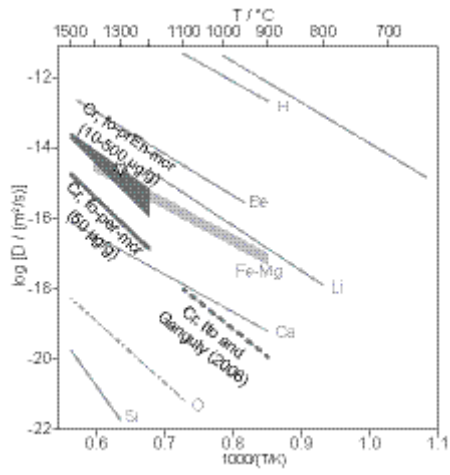
Phase or component	Formula
olivine (ol)	$(Mg,Fe)_2SiO_4$
forsterite (fo)	Mg_2SiO_4
orthopyroxene (opx)	$(Mg,Fe)_2Si_2O_6$
proto-enstatite (prEn)	$Mg_2Si_2O_6$
periclase (per)	MgO
ferropericlase* (fpr)	$\sim(Mg,Fe)O$
magnesiochromite (mcr)	$MgCr_2O_4$
Cr spinel (sp)	$(Mg,Fe)Cr_2O_4$
chromium carbide (crb)	Cr_3C_2
beta-quartz (βqtz)	SiO_2
eskolaite (esk)	Cr_2O_3

*also known as magnesiowüstite

Table 5: Abbreviations of phases and components.

	ID	$\log fO_2$ / bars or [T / °C]	Interface Cr / (µg/g)	c axis logD$_{max}$	ΔlogD	m	b axis logD$_{max}$	ΔlogD	m	a axis logD$_{max}$	ΔlogD	m
fO_2	CODE4	-0.7	1163 (44)	-13.57 (0.02)	0.67 (0.07)	134 (29)	-15.09 (0.05)	0.71 (0.06)	163 (81)	-15.53 (0.04)	0.71 (0.06)	147 (44)
	CODE11	-3.1	1219 (50)	-13.53 (0.02)	0.55 (0.02)	213 (29)	-14.83 (0.07)	0.8 (0.06)	252 (84)	-15.25 (0.05)	0.91 (0.05)	266 (36)
	CODE14	-4.6	1423 (31)	-13.42 (0.03)	0.64 (0.01)	358 (47)	n.e.	n.e.	n.e.	n.e.	n.e.	n.e.
	CODE10	-5.8	1764 (36)	-13.5 (0.02)	0.81 (0.01)	238 (18)	-14.46 (0.06)	1.01 (0.05)	461 (92)	-14.73 (0.05)	1.1 (0.02)	459 (62)
	iCODE1	-6.7*	2094 (19)	-13.4 (0.02)	0.82 (0.01)	503 (35)	-13.97 (0.35)	1 (0.2)	657 (40)	-14.39 (0.05)	0.78 (0.11)	531 (80)
	CODE16	-6.8	1890 (33)	-13.06 (0.04)	0.69 (0.03)	691 (110)	n.e.	n.e.	n.e.	n.e.	n.e.	n.e.
	CODE6a	-7.6	3089 (103)	-13.55 (0.06)	1.13 (0.05)	534 (95)	-14.26 (0.07)	1.38 (0.04)	1237 (160)	-14.59 (0.08)	1.49 (0.01)	1035 (168)
	*CODE5	-9.6	6384 (309)	-13.25 (0.03)	1.07 (0.05)	1463 (223)	-14.05 (0.02)	1.11 (0.04)	2116 (104)	-14.32 (0.05)	1.18 (0.04)	2081 (304)
	CODE3	-11.1	11289 (394)	-13.15 (0.03)	0.97 (0.01)	3491 (385)	-13.93 (0.08)	1.17 (0.08)	4020 (601)	-14.2 (0.04)	1.18 (0.02)	4064 (336)
	CODE13	-16.1	2116 (188)	-14.71 (0.01)	n.a.	n.a.	-15.67 (0.03)	n.a.	n.a.	-14.71 (0.01)	n.a.	n.a.
T	CODE12b	[1200]	2286 (576)	-14.89 (0.03)	1.15 (0.02)	391 (28)	-16.12 (0.12)	1.12 (0.14)	439 (143)	-16.8 (0.24)	0.73 (0.16)	227 (123)
	CODE8	[1306]	4264 (107)	-13.94 (0.01)	1.15 (0.01)	720 (27)	-14.74 (0.08)	1.3 (0.02)	1300 (261)	-15.01 (0.05)	1.4 (0.02)	1301 (116)
	CODE7	[1500]	11210 (323)	-12.73 (0.02)	1.02 (0.01)	2859 (173)	-13.47 (0.02)	1.15 (0.03)	3333 (139)	-13.73 (0.06)	1.17 (0.06)	3557 (726)

	ID	$\log f\mathrm{O}_2$ / bars or [T / °C]	Interface Cr / (μg/g)	c axis			b axis			a axis		
				$\log D_{max}$	$\Delta\log D$	m	$\log D_{max}$	$\Delta\log D$	m	$\log D_{max}$	$\Delta\log D$	m
$f\mathrm{O}_2$	CODE2	-0.7	39 (1)	-14.09 (0.02)	1.61 (0.07)	14 (1)	n.r.	n.r.	n.r.	n.r.	n.r.	n.r.
	CODE11	-3.1	49 (5)	-14.2 (0.11)	1.57 (0.19)	20 (6)	-15.14 (0.18)	2.05 (0.51)	64 (47)	n.r.	n.r.	n.r.
	CODE14	-4.6	57 (1)	-14.3 (0.07)	1.47 (0.04)	19 (2)	n.e.	n.e.	n.e.	n.e.	n.e.	n.e.
	CODE10	-5.8	78 (6)	-14.47 (0.13)	1.14 (0.1)	25 (9)	-15.76 (0.14)	1.27 (0.13)	26 (6)	-14.65 (0.46)	2.28 (0.51)	255 (19)
	iCODE1	-6.7	285 (57)	-13.98 (0.09)	0.19 (0.03)	597 (58)	n.e.	n.e.	n.e.	n.e.	n.e.	n.e.
	CODE16	-6.8	96 (6)	-14.66 (0.06)	1.03 (0.13)	27 (8)	n.e.	n.e.	n.e.	n.e.	n.e.	n.e.
	CODE6a	-7.6	151 (13)	-14.77 (0.03)	1.38 (0.04)	51 (4)	-13.77 (0.79)	3.15 (0.87)	531 (125)	n.r.	n.r.	n.r.
	*CODE5	-9.6	329 (21)	-14.46 (0.07)	1.19 (0.06)	112 (22)	-15.52 (0.07)	1.12 (0.1)	111 (24)	-14.71 (0.05)	1.97 (0.1)	482 (55)
	CODE3	-11.1	49 (5)	-14.14 (0.11)	1.59 (0.18)	22 (7)	-15.14 (0.18)	2.05 (0.51)	64 (47)	n.r.	n.r.	n.r.
	CODE13	-16.1	228 (24)	-16.06 (0.05)	n.a.	n.a.	-16.95 (0.15)	n.a.	n.a.	-17.42 (0.13)	n.a.	n.a.
T	CODE12b	[1200]	82 (9)	-17.05 (0.11)	n.a.	n.a.	n.d.	n.d.	n.d.	n.d.	n.d.	n.d.
	CODE8	[1306]	197 (37)	-15.33 (0.06)	1.3 (0.03)	88 (10)	-17.27 (0.08)	n.a.	n.a.	-17.79 (0.14)	n.a.	n.a.
	CODE7	[1500]	655 (28)	-13.93 (0.08)	1.08 (0.06)	238 (44)	-14.79 (0.14)	1.17 (0.04)	261 (86)	-15.15 (0.07)	1.1 (0.08)	219 (38)

Log [fO_2 /bars]	Interface concentrations / (μg/g)				Cr^{3+} diffusion	
	Cr	$Cr^{2+}/\Sigma Cr$	Cr^{3+}	Cr^{2+}	logD pair / (m^2/s)	Binding en. / (kJ/mol)
-0.7	1163 (44)	0.01 (0.001)	1151 (123)	12 (1)	-13.29 (0.03)	-81.5 (3)
-3.1	1219 (50)	0.05 (0.008)	1158 (191)	61 (10)	-13.29 (0.01)	-81.1 (1.5)
-4.6	1423 (31)	0.21 (0.026)	1124 (141)	299 (38)	-13.23 (0.03)	-77.2 (2.8)
-5.8	1764 (36)	0.34 (0.013)	1164 (50)	600 (26)	-13.24 (0.02)	-77.3 (1.5)
-6.7*	2094 (19)				-12.50 (0.37)	-43.5 (11)
-7.6	3089 (103)	0.48 (0.015)	1606 (73)	1483 (68)	-13.23 (0.10)	-59.3 (6.6)
-9.6	6384 (309)	0.81 (0.012)	1213 (61)	5171 (262)	-12.79 (0.13)	-52.3 (5.5)
-11.1	11289 (394)	0.88 (0.011)	1355 (50)	9934 (368)	-12.89 (0.04)	-62.3 (2.5)
-16.1	2116 (188)	0.98 (0.01)	42 (22)	2074 (185)		